# SEDIMENT TRANSPORT IN THE PRESENCE OF LARGE REEF BOTTOM ROUGHNESS

Andrew W. M. Pomeroy[123], Ryan J. Lowe[123], Marco Ghisalberti[45], Curt Storlazzi[6], Graham Symonds[27] and Dano Roelvink[89]

[1]ARC Centre of Excellence for Coral Reef Studies, The University of Western Australia, Australia

[2]School of Earth and Environment, The University of Western Australia, Australia

[3]The UWA Oceans Institute, The University of Western Australia, Australia

[4]Department of Infrastructure Engineering, The University of Melbourne, Australia

[5]School of Civil, Environmental and Mining Engineering, The University of Western Australia, Australia

[6]Pacific Coastal and Marine Science Center, U.S. Geological Survey, U.S.A.

[7]Centre for Australian Weather and Climate Research, CSIRO Wealth from Oceans Flagship, Wembley, Western Australia, Australia.

[8]Deltares, Delft, The Netherlands

[9]UNESCO-IHE, Delft, The Netherlands

**Corresponding Author:**
Andrew W. M. Pomeroy
School of Earth and Environment – M004
The University of Western Australia
Crawley, 6009
Western Australia

andrewpomeroy@gmail.com
+61 448 867 524



This is the author manuscript accepted for publication and has undergone full peer review but has not been through the copyediting, typesetting, pagination and proofreading process, which may lead to differences between this version and the Version record. Please cite this article as doi:10.1002/2016JC011755.

**Abstract**

The presence of large bottom roughness, such as that formed by benthic organisms on coral reef flats, has important implications for the size, concentration, and transport of suspended sediment in coastal environments. A three-week field study was conducted in approximately 1.5 m water depth on the reef flat at Ningaloo Reef, Western Australia, to quantify the cross-reef hydrodynamics and suspended sediment dynamics over the large bottom roughness (~20–40 cm) at the site. A logarithmic mean current profile consistently developed above the height of the roughness; however, the flow was substantially reduced below the height of the roughness (canopy region). Shear velocities inferred from the logarithmic profile and Reynolds stresses measured at the top of the roughness, which are traditionally used in predictive sediment transport formulations, were similar but much larger than that required to suspend the relatively coarse sediment present at the bed. Importantly, these stresses did not represent the stresses imparted on the sediment measured in suspension and are therefore not relevant to the description of suspended sediment transport in systems with large bottom roughness. Estimates of the bed shear stresses that accounted for the reduced near-bed flow in the presence of large roughness vastly improved the relationship between the predicted and observed grain sizes that were in suspension. Thus the impact of roughness, not only on the overlying flow but also on bed stresses, must be accounted for to accurately estimate suspended sediment transport in regions with large bottom roughness, a common feature of many shallow coastal ecosystems.

## 1 Introduction

The presence of large bottom roughness over coral reefs directly modifies the nearbed hydrodynamics that are responsible for sediment transport. For typical wave-exposed reefs, cross-reef mean flows (currents) are generated by radiation stress gradients induced by incident short (sea-swell) waves breaking in the surf zone (i.e., waves with periods 5–25 s) and the associated mean water level gradients (wave setup) [e.g., *Hench et al.*, 2008; *Lowe et al.*, 2009b; *Symonds et al.*, 1995]. Smaller incident waves that do not break in the surf zone are transmitted across reef flats as depth-limited waves [e.g., *Hardy and Young*, 1996], with infragravity waves that emanate from the surf zone also propagating across the reef [e.g., *Pomeroy et al.*, 2012]. The large bottom roughness of reefs can impose substantial drag forces on the mean wave-driven currents, and also attenuate wave heights by frictional dissipation as they propagate shoreward across the reef [e.g., *Lowe et al.*, 2005a; *Pomeroy et al.*, 2012; *Rosman and Hench*, 2011]. Thus, the hydrodynamic processes that prevail within reef systems are determined by the specific roughness characteristics of a reef, which in turn controls how sediment is transported in these environments.

Suspended sediment at high concentrations can adversely affect a variety of benthic reef organisms via multiple mechanisms. As sediment concentrations in the water column increase, light is attenuated and the spectrum is altered, reducing the efficiency of photosynthetic processes that many reef primary producers rely on for energy production [see *Roth*, 2014 for a review]. In addition, when the rate of sedimentation is higher than the rate at which sediment is expelled, coral communities become smothered. This inhibits biotic particle feeding and nutrient uptake rates [e.g., *Anthony*, 2000] and can eventually lead to mortality [e.g., *Weber et al.*, 2012].

For open (bare) sediment beds lacking large immobile bed roughness, the initiation of sediment transport is directly related to the shear stresses that are exerted on the sediment bed

($\tau_{bed}$). Motion is initiated when these bed stresses exceed a critical threshold that is dependent upon sediment properties, namely grain size and sediment density (i.e., as expressed in various forms of the classic Shields equation [*Shields*, 1936]). When the vertical velocity component of turbulent eddies are sufficiently large to overcome the particle fall velocity ($w_s$), sediment is lifted into suspension where it can be more efficiently transported [e.g., *Bagnold*, 1966; *Francis*, 1973; *Van Rijn*, 1984]. Vertical turbulent velocity fluctuations associated with these eddies scale with the horizontal bed stresses, or alternatively the shear velocity $\left(u_* = \sqrt{\tau_{bed}/\rho_w}\right)$ based on seawater density ($\rho_w$); therefore, relationships used to predict whether transport occurs usually depend on the magnitude of $w_s$ relative to $u_*$.

Within the water column, in a conventional steady-state 1D (vertical) model, the upward diffusion of sediment is balanced by downward settling. This diffusion is described by the vertical gradient in concentration and a sediment mixing coefficient ($\varepsilon_s$), which can be inferred from various turbulence closure models [e.g., *Van Rijn*, 1993]. Irrespective of the closure model assumed, $\varepsilon_s$ is dependent upon the turbulent shear stresses within the bottom boundary layer - the region where sediment particles are predominantly suspended and transported. Hence $\tau_{bed}$ (or $u_*$) is assumed to control many components of the overall sediment transport process, including (a) whether sediment will initially move, (b) whether that sediment will be suspended, and (c) the vertical distribution of suspended sediment concentration in the water column. Collectively, these components form the basis for modern suspended sediment transport models.

When sediment is interspersed within immobile bed roughness, such as on coral reefs as well as within aquatic vegetation such as a seagrass meadow, the mean and turbulent flow structure is substantially modified adjacent to the bed (i.e., within a 'roughness sublayer' or 'canopy', defined as the region where the flow is locally modified by individual roughness elements; [*Raupach et al.*, 1991]). While the overlying flow may experience increased

hydraulic resistance as a result of this roughness, the flow that actually interacts with the underlying bed can be substantially attenuated, which in turn reduces the bed shear stresses [e.g., *Le Bouteiller and Venditti*, 2015]. In aquatic canopies, this flow attenuation can promote sediment deposition, especially when canopy densities are high [e.g., *Gacia et al.*, 1999; *James et al.*, 2004]. A limited number of laboratory studies have quantified how sediment transport is modified by large immobile roughness. Of these studies, most only consider bulk sediment transport quantities (e.g., total transport) and do not explicitly consider how modifications to flow by roughness will alter sediment transport mechanisms that make up these bulk transport rates [e.g., *Baptist*, 2005; *Chen et al.*, 2012; *James et al.*, 2002; *James et al.*, 2004; *Kothyari et al.*, 2009]. In field experiments, the primary focus of most studies has been on how suspended sediment concentrations (SSCs) and/or suspended sediment fluxes (SSFs) measured at specific point locations in the water column are empirically correlated to the local wave and/or current conditions [e.g., *Ogston et al.*, 2004; *Storlazzi et al.*, 2009; *Storlazzi et al.*, 2004; *Suhayda and Roberts*, 1977]. Although such correlations may exist, they do not provide fundamental insight into the quantitative links between the hydrodynamic processes, immobile bottom roughness, and rates of sediment transport. Thus, the dynamics of suspended sediment transport in the presence of large roughness elements, such as coral reefs, remains poorly quantified in natural coastal environments and motivates the present study.

We hypothesize that the drag forces exerted by large immobile roughness overlying a coral reef can significantly reduce shear stresses that are directly exerted on an underlying sediment bed, and as a consequence, traditional measures of bottom stresses on a reef are poor predictors of SSCs and SSFs. The objectives of this study were to: (1) assess the 'rough-wall' boundary layer flow dynamics and turbulent shear stresses over a coral reef flat; (2) quantify the grain-size distribution and concentrations of suspended sediment in the water

column; and (3) evaluate how modifications to the mean and turbulent flow structure alter suspended sediment grain sizes, SSCs, and SSFs over a rough coral reef flat, including the implications for making robust sediment transport predictions within reef environments.

In Section 2, we review rough boundary layer theory and establish how near-bed flow and bed shear stresses are reduced within the roughness elements of a reef, and in turn how this may modify sediment transport. In Section 3, we then describe the field experiment conducted on a fringing reef, the instrument configurations, and the data analysis methodologies. The results are described in Section 4, and in Section 5 we discuss how large immobile roughness affects both SSCs and SSFs. In Section 6, we conclude with a discussion of implications of this study for making robust prediction of suspended sediment transport on coral reefs and other analogous benthic ecosystems with large bottom roughness.

## 2 Background: flow structure and sediment transport within rough-wall boundary layers

### 2.1 Unidirectional flow

A rough-wall turbulent boundary layer associated with a unidirectional current can be partitioned into an inertial sublayer and roughness sublayer (Figure 1a). The inertial sublayer, often called the logarithmic layer, develops above the roughness sublayer where the individual roughness elements no longer directly affect the flow and the mean velocity ($\bar{u}$) profile tends to be governed by the 'law of the wall' [e.g., *Raupach et al.*, 1991]:

$$\bar{u} = \frac{u_{*c}}{\kappa} \log\left(\frac{z-d}{z_0}\right) \quad (1)$$

where $z$ is height above the bed; $\kappa$ is Von Karman's constant; $d$ is the vertical displacement of the mean velocity profile that relates to the penetration of momentum into the roughness; and $z_0$ is a hydraulic roughness parameter. In Eq. (1), the shear velocity $u_{*c}$ is a measure of the

turbulent shear stress at the top of the roughness and thus is equivalent to the resistance imposed by the roughness on the overlying current (note the subscript $c$ will denote variables associated with currents).

The roughness sublayer is strongly influenced by the drag imposed by the roughness elements, which if modeled as simple geometric elements (e.g., cubes, cylinders) can be described as a function of the roughness height $h$, frontal area per unit volume $a$ and a drag coefficient $C_D$ [e.g., *Nepf et al.*, 2007]. When the bottom roughness is relatively small (i.e., $C_D ah$ is less than $O(10^{-2})$), such as over a flat sandy bed, the mean height of momentum absorption is located near the base of the roughness ($d \approx 0$) and $u_{*c} \approx u_{*c,bed}$, where $u_{*c,bed}$ is the bed shear velocity (Figure 1a). However, when the roughness is relatively large (i.e., $C_D ah$ exceeds $O(10^{-2})$), the drag forces exerted by the roughness elements attenuate the spatially-averaged flow [see reviews by *Finnigan*, 2000; *Nepf*, 2012]. This attenuation results in an inflection of the mean velocity profile at the top of the roughness where the maximum turbulent Reynolds shear stresses are also located. In this case, $u_{*c}$ in Eq. (1) no longer describes the shear stress acting on the bed, but rather the local turbulent shear stress at the top of the roughness (i.e., $u_{*c} \approx u_{*c,rough}$, Figure 1b). Thus, within the roughness sublayer (or canopy), the reduction in flow can substantially reduce the shear stresses that are exerted on an underlying sediment bed $(\tau_{c,bed})$.

### 2.2 Wave-dominated flow

When surface waves propagate over a rough seafloor, a wave boundary layer (WBL) of thickness $\delta_w$ develops close to the bed (note the subscript $w$ will denote variables associated with waves). Due to the oscillatory nature of the flow, wave-generated turbulence within the WBL can only experience limited vertical growth. A variety of forms for the eddy viscosity within the WBL have been proposed, but one of the simplest and most widely-used is that of

177 *Grant and Madsen* [1979], where a representative (time-invariant) value is assumed. Based
178 on this description, when the roughness is relatively small, $\delta_w$ is governed by the maximum
179 shear velocity imposed by the wave flow ($u_{*w}$) and the wave angular frequency ($\omega$); i.e.
180 $\delta_w \sim \kappa u_{*w}/\omega$. The thin nature of the WBL generates larger bed shear stresses $(\tau_{w,bed})$ when
181 compared to a unidirectional current of equivalent magnitude (Figure 1c).

182 Most research with waves has investigated how large roughness modifies the phase-
183 dependent wave flow structure within the canopy region. Laboratory experiments with
184 idealized canopies [e.g., *Lowe et al.*, 2005b; *Lowe et al.*, 2008; *Luhar et al.*, 2010] and field
185 experiments in seagrass canopies [e.g., *Infantes et al.*, 2012] have demonstrated that the
186 attenuation of the root-mean-squared (RMS) wave orbital velocities within the canopy is
187 always less than that of a unidirectional flow of equivalent magnitude. This is due to the
188 wave-driven oscillatory pressure gradient, which is opposed by both canopy drag and inertial
189 forces [e.g., *Lowe et al.*, 2005b; *Zeller et al.*, 2015]. Furthermore, wave phase-dependent
190 Reynolds stresses are enhanced near the top of the roughness and then decrease towards zero
191 within the canopy before they increase again near the bed [e.g., *Lowe et al.*, 2008; *Luhar et*
192 *al.*, 2010]. This stress profile suggests that for large roughness, two WBLs develop: a larger
193 WBL near the top of the canopy (or roughness layer) and another, thinner, WBL near the bed
194 (Figure 1d).

195 **2.3 Wave-current boundary layers**

196 The superposition of both waves and mean currents nonlinearly combine to modify the
197 turbulent flow structure near the bed and enhance bed shear stresses. Over a wave cycle, the
198 mean of these enhanced stresses ($\tau_m$) is larger than pure current stresses ($\tau_c$), and the
199 maximum of the enhanced stresses ($\tau_{max}$) is larger than the vector summation of $\tau_c$ and $\tau_w$
200 [e.g., *Soulsby and Clarke*, 2005].

A variety of wave-current interaction models have been proposed. Most of these models describe the turbulent flow structure over a bed with relatively small bed roughness, i.e., where the roughness height is small relative to the wave-current boundary layer thickness. These models are generally based on semi-empirical eddy viscosity profiles [see *Wiberg*, 1995 for a review]. Under combined wave-current flow, a thin WBL of thickness $\delta_{max}$ exists that is controlled by $u_{*max}$. Above this WBL ($z > \delta_{max}$), the mean velocity profile maintains a logarithmic form described by Eq. (1); however, with $u_{*c}$ instead replaced with the wave-enhanced mean velocity ($u_{*m}$) and $z_0$ replaced with an apparent roughness length ($z_{0a}$) that is also enhanced by the wave-induced turbulence near the bed relative to a pure unidirectional current [e.g., *Grant and Madsen*, 1979].

The dynamics of wave-current interactions that occur within large roughness (canopies) are still not well-established. However, it is reasonable to assume that the drag imposed by large roughness elements will cause greater attenuation of the current-component of the flow relative to the wave-component, which is supported by experimental observations [e.g., *Lowe et al.*, 2005b; *Lowe et al.*, 2008; *Zeller et al.*, 2015]. Thus, under wave-current conditions the flow within the roughness should be more strongly influenced by the contribution of the waves than the current. Similar arguments can be made to describe the flow structure near the top of the roughness and further up in the water column. At a sufficient height above a canopy, the flow structure should be analogous to a classic rough-wall wave-current boundary layer, with a logarithmic mean current profile defined by $u_{*m}$ and $z_{0a}$ that are enhanced by wave-induced turbulence generated within the canopy.

### 2.4 Sediment transport in the presence of large roughness

The total resistance experienced by the overlying flow ($\tau_{total}$) is often partitioned into two components: (1) a bed stress component ($\tau_{bed}$) that is due to the stress imposed by sediment grains at the bed; and (2) a form drag component $\left(\tau_{drag}\right)$ that is due to drag forces either by

mobile bed forms [e.g., *Van Rijn*, 2007] or by immobile roughness (e.g., coral structures or aquatic vegetation [e.g., *Le Bouteiller and Venditti*, 2015].

$$\tau_{total} = \tau_{bed} + \tau_{drag} \quad (2)$$

In the presence of relatively small roughness (e.g., the sand grains themselves), $\tau_{drag}$ is small and $\tau_{total} \approx \tau_{bed}$; thus the shear stress exerted on overlying flow is equally relevant to the assessment of sediment transport. However, when the roughness is large, $\tau_{drag}$ can be substantially greater than $\tau_{bed}$; in this case the shear stress estimated from hydrodynamic measurements obtained higher in the water column, which includes the large form drag exerted by the roughness (i.e., $\tau_{total}$), is not necessarily related to the stress exerted on the sediment. This has been demonstrated in idealized laboratory experiments where stresses inferred from law-of-the-wall fitting of the velocity profile above roughness have been shown to significantly overestimate bedload sediment transport [e.g., *Le Bouteiller and Venditti*, 2015], as well as the capacity of a unidirectional flow to suspend and transport sediment when compared to the same flow over a bare sediment bed [e.g., *Bouma et al.*, 2007]. Thus, while the mobilization and suspension of sediment from the bed is broadly governed by the same physical processes (irrespective of whether the roughness is either large or small), these key differences between bed shear stresses should have important implications for rates of sediment transport, and notably the applicability of existing predictive formulae to environments with large roughness.

## 3 Methods

### 3.1 Site Description

A 3-week field experiment (27 July–14 August 2013) was conducted in the northern region of Ningaloo Reef in Western Australia, focusing on a ~5 km section of reef near Tantabiddi (21°52'6"S, 113°58'58"E, Figure 2a). The study specifically focused on a section of reef bounded to the north and south by shore-normal channels (~6 m deep) that cut into the reef

crest and outer reef flat. At this site, the cross-shore orientation of the reef is ~130° (defined as clockwise from true north), with the reef crest located 2.0–2.5 km from the shoreline. The reef flat is ~0.6–1.5 m below mean sea level and is ~500 m wide. The lagoon varies in width along the coast due to the presence of a shoreline salient, and is generally ~3 m deep. In contrast to many parts of southern Ningaloo Reef that typically have near 100% coral coverage, this site was specifically chosen as, like many reef systems worldwide, it contained a mix of macro-algae, coralline algae, sand, and some live coral [*Cuttler et al.*, 2015].

### 3.2 Field Study

The field study consisted of two main components: (1) a detailed study of the hydrodynamics and sediment transport of the reef flat, and (2) a broader-scale hydrodynamic and sediment transport study throughout the reef and lagoon [*Pomeroy*, 2016]. The results presented in this paper focus on the first component, which was based on intensive sampling conducted on the reef flat (S2, Figure 2b) that was designed to quantify the fine-scale sediment dynamics over the reef.

A 'sawhorse' instrument frame was deployed at S2 in a water depth of ~1.5 m (Figure 2e,f). Here the bed roughness is ~20–40 cm high. Hydrodynamic measurements were obtained using three vertically-distributed Nortek acoustic Doppler velocimeters (ADVs). The bottom ADV was located within the roughness sublayer ($z$ = 0.2 m), the middle ADV was located near the top of the roughness elements (z = 0.5 m) and the top ADV was located high in the water column (z = 0.8 m). The ADVs sampled at 8 Hz for 2048 s each hour. In addition to the ADVs, an upward facing Nortek high-resolution acoustic Doppler profiler (ADP) located slightly to north (~2 m) of the sawhorse frame sampled continuously at 1 Hz using 25 mm bins with the bottom bin located 0.22 m above the bed. Suspended sediment concentrations were inferred from three WetLabs ECO-FLNTU optical backscatter sensors (OBSs) that sampled at 0.3 Hz for 20 min each hour. Suspended sediment samples were

collected *in situ* using a suction sampling array that consisted of six 5 mm diameter intakes that were vertically positioned with logarithmic spacing, oriented perpendicular to the dominant mean flow direction, with water pumped to a scaffold platform nearby. Based on the intake diameter and volume flow rate, the intake flow velocity was approximately 0.6 m $s^{-1}$, or 2–3 times greater than measured root-mean-squared (RMS) velocities (see below); therefore, errors due to inefficiencies or bias in particle capture are expected to be small [*Bosman et al.*, 1987]. A summary of the instrumentation and sampling information is provided in Table 2.

In an ~40 m x 40 m region surrounding the sawhorse frame, a fine-scale topographic survey was used to quantify the bottom roughness. The bathymetry was measured (Figure 2c) with single-beam acoustic sonar (Humminbird 798c) and supplemented with four manually-measured roughness transects spaced at ~1.5 m horizontally (Figure 2d). Each manual transect was defined by an 8 m wire that was tensioned and levelled. The distance between the bed and the wire was measured every 1 m horizontally with 1 cm vertical resolution. The roughness survey indicates that the coverage in benthic roughness varied and consequently the roughness characteristics were somewhat patchy with slightly larger roughness elements (in vertical dimension) located upstream of the sampling site.

### 3.3 Data Analysis

#### 3.3.1 Hydrodynamic data

Offshore wave conditions (wave height, period and direction) were measured on the forereef (S1) using a Nortek acoustic wave and current meter (AWAC) with acoustic surface tracking (AST); whereas wave conditions on the reef flat were obtained from pressure time series converted to surface elevations using linear wave theory. From the wave spectra, the root-mean-squared (RMS) wave-heights for the shorter-period (5–25 s) sea-swell waves ($H_{rms,sw}$)

and longer period (25–250 s) infragravity ($H_{rms,ig}$) waves, as well as the peak period $(T_p)$, were calculated through integration of the energy within these respective bands.

The raw ADV and ADP velocity measurements were initially filtered based on low signal correlations (< 60%) before velocity spikes (e.g., caused by bubbles or debris in the sample volume) were removed using a kernel-based despiking algorithm [*Goring and Nikora*, 2002]. The direction of the waves and currents were computed separately so that the angle between the waves and currents could be considered in the calculation of the bed shear stresses imposed by the wave-current boundary layer. For each 15-minute burst of data, the mean current ($\bar{u}$) speed and direction were computed. The reef flat free-stream velocity ($\bar{u}_\infty$) was defined as the depth-averaged current speed of the top five ADP cells unaffected by the free surface (i.e. roughly 0.7–0.8 m above the sediment bed). The mean current vector was then removed from each velocity record and the (residual) oscillatory velocity data rotated into a coordinate system that maximized the velocity variance along the primary axis. In this coordinate system, the wave ($\tilde{u}$) and RMS velocities ($\tilde{u}_{rms}$) were determined.

Across a range of conditions, a logarithmic velocity profile was consistently observed within a region approximately 0.5–0.8 m (~12 data points) above the bed (Figure 3). Above the upper height, the flow profile at times deviated from a logarithmic form as it approached a free-stream velocity; below the lower height, the flow profile was often inflected, consistent with a canopy flow (e.g., Figure 1). This transition towards the in-canopy flow occurred at an elevation that was comparable to the measured height of the roughness near the site (~20–40 cm). To determine the mean shear velocity above the roughness sublayer $(u_{*m,rough})$ for the combined wave-current flow (see Section 2.3), a least-squares best fit of Eq. (1) against the time-averaged 15 min bursts of the ADP data within the logarithmic region (0.5–0.8 m above bed) was conducted. To ensure a robust logarithmic profile existed, we only retained

estimates of $u_{*m,rough}$ from profiles with a $R^2 > 0.95$, with the vast majority (~90%) of the bursts satisfying this criterion. The boundary layer theory of *Grant and Madsen* [1979] and the implementation described by *Madsen* [1994] was used to calculate $u_{*max,rough}$. We used $\bar{u}$ and $u_{rms}$ measured above the logarithmic layer ($z = 0.8$) and the $z_{0a}$ from the logarithmic fit to define an equivalent Nikuradse roughness (i.e., $k_N = 30z_{0a}$).

Estimates of $u_{*m,rough}$ were compared to those calculated from the turbulence data measured by the ADVs. Here we further separated the measured horizontal and vertical data into wave ($\tilde{u}$ and $\tilde{w}$) and turbulent velocity ($u'$ and $w'$) components. We used data from the top and middle ADVs for this decomposition, whereby the turbulent motion was obtained by removing correlated motions between the two instruments (i.e., waves) [*Shaw and Trowbridge*, 2001]. The mean shear velocity enhanced by waves and currents was then determined from the Reynolds stresses $\left(u^2_{*m,rough} = -\overline{u'w'}\right)$ at the middle ADV ($z =$ 0.5 m). At this elevation, the Reynolds stresses are expected to be slightly below the inertial sublayer (logarithmic) region and representative of the shear velocity just above the roughness elements.

The bottom ADV located below the roughness height was of poorer quality, so it was only used to evaluate the mean current and wave velocities, but not to obtain direct estimates of the Reynolds stresses. To estimate the magnitude of the mean $\left(u_{*m,bed}\right)$ and maximum wave-current shear velocity $\left(u_{*max,bed}\right)$ at the sediment bed (at the base of the canopy, Figure 1d), we again used the approach described by *Madsen* [1994] but now with the velocities measured by the bottom ADV. For this flow within the canopy, the roughness was defined with the Nikuradse sand grain roughness ($k_N = 2.5D_{50}$) determined from the median bed grain size measured at the bed level between the roughness elements ($D_{50} \cong 240$ μm, Figure 8b).

### 3.3.2 Suspended sediment grain sizes and concentrations

Suspended sediment grain sizes and concentrations were determined from suction samples at hourly intervals during daylight hours. The water samples were collected with peristaltic pumps via intake ports located perpendicular to the dominant cross-reef flow direction [*Bosman et al.*, 1987] and stored in 2 L bottles. The samples were vacuum filtered onto pre-weighed membrane filters (Whatman ME27, 0.8 μm), dried (75°C for 24 hrs) and weighed in order to calculate SSCs. The dried filters were then imaged under a microscope to obtain ~50 evenly spaced images of the filter surface that were obtained with an accuracy of 2 pixels : 1 μm. For each image, the sediment grains were manually identified under a microscope and their location recorded on the image. A Canny edge detection algorithm [*Canny*, 1986] was then used in MATLAB to detect the edge of the particles in each image based on local maxima of the image intensity gradient. The largest and smallest dimension of the irregularly shape particles was manually identified in order to determine the size of the particles. Particles with dimensions <50 μm were omitted, as it was often difficult to identify a clearly defined particle boundary and thus these particles could not be reliably measured.

To relate the suspended sediment grain size distribution to the shear stresses above and within the canopy, we determined the equivalent grain size that could be suspended by a given shear velocity based on the downward particle fall velocity ($w_s$):

$$\frac{u_*}{w_s} = \alpha \tag{3}$$

where $\alpha$ represents the different stages of suspension and ranges from bursts of sediment in suspension when $\alpha \leq 1$ to fully-developed suspension when $\alpha \gg 1$ [*Bagnold*, 1966; *Van Rijn*, 1984]. Note that this ratio is related to the inverse of the Rouse number. We set $\alpha = 1$ based on the following arguments: (1) For a specific grain size to be suspended from the bed it must have experienced a shear stress that was sufficient to enable it to be mobilized from

the bed. (2) For the range of sediment grain sizes measured in suspension in this experiment, once these grains are mobilized they (theoretically) directly enter a state of suspension [e.g., *Bagnold*, 1966; *Francis*, 1973]. (3) The state of suspension (i.e., whether sediment is in a burst or fully-developed suspension) is not relevant for the current analysis. Here we use the *Soulsby* [1997] formulation to estimate $w_s$ as:

$$w_s = \frac{\nu}{D}\left(\sqrt{10.36^2 + 1.049D_*^3} - 10.36\right) \quad (4)$$

where $\nu$ is the kinematic viscosity of the water $\left(9.35 \times 10^{-7}\text{m}^2\text{s}^{-1}\right)$, $D$ is the particle size of interest and $D_*$ is the dimensionless grain size $\left(D_* = (g(s-1)/\nu^2)^{1/3}D\right)$ with $g$ the gravitational acceleration constant and $s$ is the ratio of the carbonate sediment grain density $\left(\rho_s = 2600\text{ kg m}^{-3}\right)$ estimated by gravitational displacement [*Cuttler et al.*, 2015] to water density $\left(\rho_w = 1026\text{ kgm}^{-3}\right)$ from sediment samples obtained at the site.

The OBS and ADP backscatter data were calibrated with the SSC measurements obtained by suction sampling. The known SSCs obtained through filtration were related via linear regression (Table 3) to the measured backscatter, time-averaged over the duration when the suction samples were obtained. For the OBS instruments, the suction sample intake port that was closest (vertically) to the optical measurement elevation was used in the calibration, whereas for the ADP data (corrected for acoustic decay [e.g., *Ha et al.*, 2011]) we related three measurement cells to their adjacent intake ports and then applied the mean linear-fit equation to the data. The Root Mean Squared Error (RMSE) of the calibrated OBS and ADP backscatter was ~0.20 mg $L^{-1}$ for all instruments, except for the middle OBS that was slightly lower (~0.13 mg $L^{-1}$); these errors were much smaller than the typical measurements that ranged from 0.5–8 mg $L^{-1}$ (Section 4.2.2). The calibrated backscatter therefore provided a reasonably accurate measure of SSCs in this experiment due to the

narrow distribution of fine sediment at low concentration that we observed (see below) [e.g., *Francois and Garrison*, 1982; *Richards et al.*, 1996].

## 4 Results

### 4.1 Hydrodynamic conditions

During the first part of the experiment (1–5 August 2013), the offshore RMS wave heights ($H_{rms,sw}$) measured on the forereef at S1 were small and relatively consistent (~0.5–0.8 m, Figure 4b). Two larger swell events (6–8 August 2013 and 9–11 August 2013) occurred during the latter part of the experiment, with maximum wave heights reaching ~1.7 m during both events. Peak periods ($T_p$) ranged from 12 s during lower wave conditions to up to 19 s during the larger swell events (Figure 4b). There was a large reduction in sea-swell wave heights ($H_{rms,sw}$) on the reef flat at S2 (Figure 4d). Variations in the water depth, predominantly driven by the tide (Figure 4a,c), strongly modulated $H_{rms,sw}$ on the reef flat through depth-limited wave breaking (Figure 4d); however, the infragravity wave heights ($H_{rms,ig}$) were not strongly modulated by the water depth, responding much more to the offshore $H_{rms,sw}$. As a consequence, the $H_{rms,sw}$ on the reef flat were larger than $H_{rms,ig}$ during high tide, but were similar or smaller than $H_{rms,ig}$ at low tide during the larger swell events.

Mean free-stream current velocities ($\bar{u}_\infty$) on the reef flat varied in response to the offshore wave conditions (~0.05–0.45 m s$^{-1}$) as a result of the dominant wave-driven currents on the reef flat, with only small variability associated with the tides (typically by ±0.05 m s$^{-1}$) (Figure 4e). Thus, during the first part of the experiment the flows tended to be dominated by wave orbital velocities ($\bar{u}_\infty/\tilde{u}_{rms} < 1$, where $\tilde{u}_{rms}$ is the RMS value of the wave velocity, Figure 4f). At low tide, the combined effect of smaller waves and the relative increase in mean flow resulted in mixed wave-current conditions ($\bar{u}_\infty/\tilde{u}_{rms} \sim 1$). During the larger offshore swell events, due to the depth-limitation of wave heights on the reef flat and stronger

wave-driven mean currents, the reef flat became current-dominated ($\bar{u}_\infty/\tilde{u}_{rms} > 1$) over much of this period.

### 4.1 Flow structure and turbulent stresses

#### 4.1.1 Above the roughness

The mean current profile above the roughness was consistently logarithmic over the full range of current and wave conditions (~90% of the data conformed to Eq. (1) with an acceptance threshold of $R^2 > 0.95$). The mean shear velocities $(u_{*m,rough})$ estimated from Eq. (1) usually agreed well with those derived from the ADV-derived Reynolds stresses throughout the experiment (Figure 5a). When these $u_{*m,rough}$ values are converted to a bottom friction coefficient ($C_f = u^2_{*m,rough}/\bar{u}^2_\infty$), the mean value for the duration of the experiment was 0.035 (standard deviation 0.012). These $C_f$ are within the range (O(0.01)) that are typically reported for other reef flats [e.g., *Lowe and Falter*, 2015 for a review]. This suggests that the dynamics observed in this experiment are unlikely to be unique to this site.

Values of $u_{*m,rough}$ estimated from the log-fitting increased approximately linearly with mean current speed and were maximum when $\bar{u}_\infty \sim 0.3$ m s$^{-1}$; however, appeared to slightly decrease slightly for the largest values of $\bar{u}_\infty$, albeit with more scatter (Figure 5b). Furthermore, for a given value of $\bar{u}_\infty$, $u_{*m,rough}$ increased as the hydraulic roughness ($z_{0a}$) increased. This increase in $z_{0a}$ occurred as the conditions became more wave-dominated (Figure 5c). The increase in both $u_{*m,rough}$ and $z_{0a}$ under stronger wave conditions is consistent with the enhancement of the mean bottom stresses (and apparent bottom roughness) by waves. We note that the current direction varied slightly throughout the experiment (only by ±10–20°), thus changes in upstream roughness may also affect the estimated bottom stress and could account for some of the scatter observed.

#### 4.1.2 Within the roughness

Within the roughness (canopy) region, there was greater attenuation of the mean current relative to free stream values when compared to the wave velocities (Figure 6). In this near-bed region, the currents were generally reduced to only ~25% of the free-stream velocity (Figure 6a,b), whereas the RMS wave velocities generally remained ~75% of the free stream values (Figure 6c,d).

The estimated mean shear velocity imposed on the underlying sediment bed ($u_{*m,bed}$) was approximately four times smaller than the mean shear velocity at the top of the roughness ($u_{*m,rough}$, Figure 7a). Similarly, the maximum wave-induced shear velocity was much larger at the top of the canopy ($u_{*max,rough}$) than at the bed ($u_{*max,bed}$, Figure 7b). When the shear velocities at the bed were compared, $u_{*max,bed}$ was approximately twice as large as $u_{*m,bed}$ (Figure 7c). We note here that while there is some spatial variability in the velocity measured by the ADV and ADP (Figure 6), likely due to fine-scale spatial variations in the roughness, this velocity variability is small. Thus, any differences in shear stresses estimated by the ADV and ADP will also be small, relative to the large vertical differences in the shear stress (i.e., at the bed and at the top of the canopy).

### 4.2 Suspended sediment

#### 4.2.1 Grain size distributions

The grain size distributions obtained from the suction samples were similar across the various samples analyzed in the experiment. Although a small number of larger grains were identified in the microscope analysis, ~50% of the grains were within the range of 60–85 μm, with a typical median grain size ($D_{50}$) of ~70 μm (Figure 8a). We expect there to be some material that is finer than 50 μm (the lower limit of the analysis) that would shift the median slightly finer; however, we only observed a very small amount of material at 50 μm, so we do

expect this contribution to affect the results. The maximum contribution of the larger grains (>150 μm) was consistently less than 10% for each of the analyzed samples. This is in contrast to the distribution of the bed sediment at this site, which was dominated by much coarser sediment mostly ranging from ~150–500 μm ($D_{50}$ = 240 μm) (Figure 8b).

The $u_{*m,rough}$ was predicted to be well-beyond what was needed to maintain much of the bed sediment in suspension, as determined from the fall velocity in Eq. (3) (red solid line, Figure 8b); however, these larger grain sizes were notably absent from the water column (Figure 8a). The absence of these large size fractions in suspension indicates that the shear stress applied to the sediment was substantially smaller than the mean shear at the top of the roughness. This discrepancy is even greater if we consider $u_{*max,rough}$, which would be capable of suspending sediment up to $D_{50}$=550-1000μm (off the scale in Figure 8a).

The grain sizes observed in the water column were much closer to the equivalent grain size that could be maintained in suspension by $u_{*m,bed}$ (blue solid line, Figure 8a). However, we also note that a substantial proportion of the suspended sediment distribution remained above this estimate. If the enhanced shear velocity due to waves $(u_{*max,bed})$ is considered, the range of grain sizes that could be maintained in suspension encompasses almost the entire suspended sediment distribution that was observed (blue dashed line, Figure 8a).

The relationship between the shear velocities and the measured SSC samples were also consistent throughout the duration of the experiment: $u_{*m,rough}$ was sufficient to suspend the observed $D_{50}$ that was in suspension and the seabed $D_{50}$ during the swell events; $u_{*max,rough}$ was consistently large enough to suspend the seabed $D_{50}$ (Figure 8c). Within the roughness, $u_{*m,bed}$ alone was sufficient to suspend the observed $D_{50}$ that was in suspension, however the addition of the wave component of the enhanced bed stress is clearly evident

throughout the time series but remained insufficient (except at the peak of the swell events) to suspend the seabed $D_{50}$ (Figure 8d).

### 4.2.2 Sediment concentrations and fluxes

The calibrated ADP and OBS backscatter data were consistent with the SSCs measured directly by suction sampling throughout the experiment (Figure 9a-c). Early in the experiment when the waves were low (1–6 Aug), the SSC varied from ~0.5 mg $L^{-1}$ at low tide to ~2–3 mg $L^{-1}$ at high tide. During the larger swell events spanning 5–8 Aug and 9–12 Aug, the SSCs were consistently higher and peaked at ~8 mg $L^{-1}$ but continued to vary with tidal phase.

The form of the concentration profile defined by the ADP backscatter and the suction samples was grouped according to four hydrodynamic conditions: (I) low offshore waves and rising tide (Figure 9d), (II) low offshore waves and falling tide (Figure 9e), (III) high offshore waves and rising tide (Figure 9f) and (IV) high offshore waves and falling tide (Figure 9g). For condition (I), no direct suction samples were obtained during the field experiment, so only profiles derived from the calibrated ADP are shown. For each of the remaining conditions, the time-averaged SSC profile inferred from the calibrated ADP backscatter was comparable in structure to the mean SSC profile described by the suction samples. Each concentration profile exhibited similar features: near the bed, the concentration was low but increased slightly with height above the bed; then above the roughness sublayer, a near constant concentration was observed. There was a very strong relationship between the depth-integrated SSC within the roughness ($z = 0.2-0.4$ m) and both $u_{*m,bed}$ and $u_{*max,bed}$ (Figure 10). However, no clear relationship was observed when $u_{*m,bed}$ was small (<0.005 m $s^{-1}$), i.e. when the wave contribution was also small.

## 5 Discussion

Few studies have directly measured sediment transport over large roughness, especially in a natural field setting. However, the presence of roughness has been thought to decrease sediment transport rates through the attenuation of velocity and turbulence within the roughness sublayer (i.e., the canopy) in terrestrial [e.g., *Prosser et al.*, 1995], riverine [e.g., *Neary et al.*, 2011], and estuarine [e.g., *Ward et al.*, 1984] environments. Of the studies that have specifically considered sediment transport within canopies, most have been from unidirectional laboratory-based experiments that only consider bulk sediment transport rates from changes in the bed morphology or sediment traps, with most attention also focused on emergent canopies [e.g., *Baptist*, 2005; *Jordanova and James*, 2003; *Le Bouteiller and Venditti*, 2015; *Widdows et al.*, 2008]. This present study provides new quantitative insight into how suspended sediment grain sizes, SSCs, and SSFs are modified by the presence of submerged roughness on a coral reef flat that is subject to both waves and currents.

Typically, field studies conducted on reefs have empirically related sediment transport rates to shear velocities estimated from hydrodynamics measurements above the roughness (i.e. a measure of the total flow resistance, including the effect of form drag) [e.g., *Ogston et al.*, 2004; *Presto et al.*, 2006]. In this present study we make a direct connection between the observed suspended sediment grain sizes and the reduced hydrodynamic forces present at the sediment bed at the base of the immobile roughness. From these suspended sediment observations, we then determined the shear velocity at the bed required to suspend the observed sediment. Both the mean ($u_{*m,rough}$) and maximum ($u_{*max,rough}$) shear velocities determined from the hydrodynamics above the roughness layer were approximately an order of magnitude larger than those required to suspend the observed grain sizes within the bed, despite none of this material being observed in suspension. Therefore, $u_{*m,rough}$ and $u_{*max,rough}$ were poor predictors of the actual sediment grain sizes that were observed in

suspension, whereas estimates obtained using the reduced bed friction velocities ($u_{*m,bed}$ and $u_{*max,bed}$) were much more consistent with the observations.

Although some studies have previously considered how large immobile roughness on the bed can reduce overall bulk sediment transport rates [e.g., *Bouma et al.*, 2007; *Le Bouteiller and Venditti*, 2015], how this roughness influences suspended sediment transport has remained poorly understood. In the present study, $u_{*m,bed}$ was still not large enough to explain the suspended sediment $D_{50}$. However, when $u_{*max,bed}$ was considered, almost the entire range of the observed suspended sediment grain sizes were predicted to be in suspension. This suggests that the range and relative proportions of grain sizes in suspension are explained by the wave orbital velocities within the roughness (canopy), and also differences between how wave and current motions dynamically interact within a canopy.

### 5.1 The influence of roughness on suspended sediment concentration profiles

The observation of persistently elevated sediment concentrations near the top of the roughness, relative to values near the bed, contrasts with a multitude of observations in other environments (e.g., beaches and rivers) of monotonically decreasing concentration with height above the bed. While this profile may at first appear counter-intuitive, the hydrodynamic influence of the large roughness provides a possible explanation (explored in this section) for the development of this profile.

In flow over an erodible bed for which the ratio $w_s$ / $u_*$ is small, sediment will be entrained from the bed into the water column, where it will be transported (advected) as suspended sediment. At equilibrium, sediment suspension balances sediment deposition; otherwise, the sediment concentration will vary with streamwise distance until an equilibrium profile is attained. The distribution of sediment in suspension is typically modelled as a vertical diffusive process, which can be described by the advection-diffusion equation:

$$\underbrace{\frac{\partial(uc)}{\partial \mathrm{x}}}_{1} - \underbrace{\frac{\partial(w_s c)}{\partial \mathrm{z}}}_{2} - \underbrace{\frac{\partial}{\partial \mathrm{z}}\left(\varepsilon_s \frac{\partial \mathrm{c}}{\partial \mathrm{z}}\right)}_{3} = 0 \tag{5}$$

In Eq. (5), Term 1 describes the horizontal advection of sediment, Term 2 gravitational settling and Term 3 the vertical diffusion of sediment. Here, $\varepsilon_s$ is the sediment mixing (diffusion) parameter, which can be approximated (in various forms) as a function of the turbulent eddy viscosity ($\nu_t$) or $u_*$ [e.g., *Van Rijn*, 1984].

The development of suspended sediment concentration profiles over erodible beds with and without roughness is obtained by solving Eq. (5) with an upwind numerical scheme. We consider the case of a uniform sediment concentration upstream of the roughness ($c_{x=0}$) due to, e.g., wave breaking in an upstream surf zone. To solve Eq. (5), two boundary conditions are required: (i) at the upper boundary (the free surface) there is zero vertical flux, and (ii) at the bed ($z = 0$), the upward diffusive flux balances gravitational settling (i.e., $w_s \mathrm{c} = -\varepsilon_s \, \partial \mathrm{c}/\partial \mathrm{z}$). Typically, a near-bed reference concentration ($c_0$) is used to specify this bottom boundary condition. Many formulations have been developed for $c_0$, most of which functionally depend on the shear stress applied to the sediment bed [e.g., *Lee et al.*, 2004; *Smith and McLean*, 1977]. Here, we specified a spatially-constant (i.e., in the stream-wise direction x) $c_o$ using the formulation proposed by *Lee et al.* [2004]:

$$c_0 = A\left[\theta \frac{u_*}{w_s}\right]^B, \tag{6}$$

where $c_0$ is defined at a reference height $z_{ref} = 0.01$ m above the bed, $\theta$ is the grain roughness Shields parameter and $u_*$ is the shear velocity at the sediment bed. We use $A$ = 2.58 and $B$ = 1.45 for the two empirically-derived constants, but recognize that there is some uncertainty around these values [*Lee et al.*, 2004].

For comparison, we first determine the concentration profile over a bare erodible bed (i.e. without roughness). Typical values of the uniform mean current ($\bar{u} = 0.3$ m s$^{-1}$), uniform grain size in suspension (70 μm) and bed friction velocity ($u_* = 0.08$ m s$^{-1}$) are used. The sediment diffusivity ($\varepsilon_s$) is assumed to increase linearly with height above the bed (i.e. $\varepsilon_s = \nu_t = \kappa u_{*max,rough} z$, Figure 11a). With this diffusivity profile, the initially uniform concentration profile, which in this example we initialize with $c_0$, evolves downstream to form a classic exponentially-decaying profile above the bed (Figure 11b).

In this study, we typically observed a four-fold difference between $u_{*max,rough}$ and $u_{*max,bed}$ due to the large bottom roughness. The presence of large roughness therefore has two important modifications to the solution to Eq. (5). Firstly, $\tau_{bed}$ is reduced and consequently so is $c_0$. For comparison with the bare bed case, we assume the same maximum value of $u_*$ here at the height of the roughness (i.e. $u_{*max,rough}$= 0.08 m s$^{-1}$) and a reduced value for $u_{*max,bed}$ (which is used in Eq. 6 to determine $c_o$) of 0.02 m s$^{-1}$; as a consequence $c_0$ is also lower in the presence of the roughness. Secondly, flume experiments have shown that in unidirectional flow over large roughness, the turbulent diffusivity decreases linearly from a maximum value near the top of the roughness to a diminished value deep within the roughness [e.g., *Ackerman and Okubo*, 1993; *Ghisalberti*, 2007; *Ghisalberti and Nepf*, 2004]. Accordingly, a two-layer distribution of $\varepsilon_s$ was assumed here (Figure 11a), where $\varepsilon_s$ is lower within the roughness than above it.

The solution to Eq. (5) in the presence of large roughness was obtained by assuming the same uniform mean current, suspended sediment grain size, and the initializing condition as in the bare bed case. For this case, the SSC profile evolves from the uniform upstream concentration to a shape where the concentration increases with height above the bed (Figure 11b). This is qualitatively consistent with the SSC profiles observed in this experiment

(Figure 9). Eventually (far downstream) the solution will converge to an exponential profile, analogous to that observed over a bare sandy bed but with a much lower concentration; for the fine suspended sediments (low settling velocity) observed in this study, that development would occur over large distances.

Thus, a likely explanation for the SSC profiles observed in the field experiment is that the narrow but aggressive surf zone located ~400 m upstream near the reef crest initially creates a well-mixed distribution of fine suspended sediment that slowly settles out of the water column. This sediment is advected by the cross-reef mean flows over and within the roughness. The reduced bed shear stress within the roughness leads to a reduction in $c_o$, resulting in a net downward sediment flux by both diffusion and gravitational settling; the divergence in the vertical sediment flux is balanced by a convergence in the horizontal advective flux. It is this reduction in $c_o$ when compared to a larger upstream concentration that results in the reduced SSC values near the bed. These results suggest that the fine sediments ($D_{50}$ = 70 μm) observed in suspension would likely include contributions from both local resuspension and sediment sourced upstream by advection. The fact that the coarse local bed sediment ($D_{50}$ = 240 μm) is not in suspension is also consistent with this model, as the reduced bed shear stress within the roughness was found to be incapable of suspending this coarse sediment fraction.

### 5.2 Estimated versus measured suspended sediment fluxes

Physical relationships that describe the hydrodynamics of bare sandy beds are still regularly applied to obtain quantitative estimates of sediment transport within ecosystems with large bottom roughness. It is therefore of particular interest to assess the sensitivity of predictions of SSFs (which integrate the effects of the modified concentration and velocity profiles), to these different definitions of the shear velocity. It is not our intention to conduct an exhaustive review of the applicability of key formulae, but instead to apply the different $u_*$

627 values from this study in a one-dimensional (vertical) concentration profile model to simply
628 assess the sensitivity of SSF predictions.

629 The depth-integrated Eulerian-mean SSFs were calculated from local estimates of
630 SSF ($\bar{u}\bar{c}$) that were determined from time-averaged concentrations ($\bar{c}$) measured directly from
631 the suction sample array and the co-located current velocity data ($\bar{u}$) measured at the time of
632 sediment sampling by the ADP. We assume that the SSF at the lowest measurement point
633 was representative of the fluxes further below, but recognize the flux could also be higher in
634 this region. These discrete estimates were supplemented with SSFs calculated using 15-min
635 bursts of velocity and the indirectly measured SSCs (calibrated backscatter) from the ADP.

636 In order to predict the SSF for different $u_*$ values, a SSC profile must be determined,
637 which in turn requires prescription of the near-bed reference concentration ($c_0$). We specify
638 the reference concentration using the same empirical model of *Lee et al.* [2004] used earlier
639 (Eq. 6). The form of the SSC profile is commonly represented by various solutions to Eq. (5)
640 (e.g., exponential, power law, Rouse). We note that such SSC profiles only consider the
641 diffusion and gravitational settling of sediment and do not take into account the advection of
642 sediment from other areas. Here, a commonly employed power-law formulation was used:

$$c(z) = c_0 \left( \frac{z}{z_{ref}} \right)^{-P} \tag{7}$$

643 where z is the height above the bed and $P = w_s/\kappa u_{*,max}$ is the Rouse parameter. We note
644 that this formulation results in a lower SSC higher in the water column than at the bed, which
645 is not consistent with the observations in this experiment. However, we re-emphasize here
646 that the purpose of the present analysis is to evaluate the extent to which the SSF estimates
647 from established approaches (such as the one described by Eq. (7)) may deviate from the

observations to assess the errors that can be introduced by applying conventional sediment transport formulations to these environments.

The horizontal velocity ($\bar{u}$) used to estimate the SSF was based on values measured by the ADP and we determined the SSFs following what was done earlier with the field data. We evaluated four cases, where the $u_*$ that was used to calculate $c_0$ taken as either $u_{*max,rough}$ or $u_{*max,bed}$ and with the sediment grain size as either the $D_{50}$ in suspension (70 μm) or the seabed $D_{50}$ (240 μm). The shear velocity used to calculate the Rouse parameter was $u_{*m,rough}$, which represents the greater mixing expected in the water column.

With the $D_{50}$=70 μm observed in suspension, the SSFs estimated using $u_{*max,rough}$ are three orders of magnitude larger than those observed (Figure 12a), while for the seabed $D_{50}$=240 μm the estimated SSF is approximately 1–2 orders of magnitude too large (Figure 12b). In contrast, the SSF estimated using the reduced $u_{*max,bed}$ within the roughness and $D_{50}$ =70 μm observed in suspension was of the correct order of magnitude (Figure 12c), an agreement that persisted throughout the experiment (Figure 12e). The SSF estimated with the reduced $u_{*max,bed}$ and the seabed $D_{50}$ =240 μm was underestimated by 1–2 orders of magnitude (Figure 12d).

This sensitivity analysis demonstrates that established methods used to estimate SSF will substantially overestimate the flux when the shear stresses are estimated from hydrodynamic measurements that include the large form drag exerted by the roughness (i.e., when the impact of the roughness layer is not specifically considered). However, if the flow structure within the roughness is considered, the estimated SSF for this experiment was much closer and of the correct order of magnitude when the appropriate $D_{50}$ in suspension is considered.

### 5.3 Implications for sediment transport predictions

Existing studies of sediment dynamics in benthic ecosystems with large bottom roughness (e.g., coral reefs) still tend to focus on the long-standing framework for how sediment dynamics operate over bare sediment beds (e.g. as occurs on sandy beaches). There have been considerable advances in predicting how hydrodynamic processes in coral reefs are modified by the presence of large bottom roughness (i.e., how the roughness affects circulation and wave transformation) with emphasis in these hydrodynamic studies generally on correctly representing the hydrodynamic properties above the roughness. This has typically been achieve by adjusting empirical friction parameters (e.g., by adjusting bottom drag coefficients in models to account for the large bottom roughness [e.g., *Lowe et al.*, 2009a; *Van Dongeren et al.*, 2013]). While this approach may yield a more 'correct' reproduction of the hydrodynamic processes (at least above the canopy), this approach will greatly overestimate the bed stresses that act on the sediment, which are directly responsible for driving sediment transport. Therefore, while the presence of the large roughness has the effect of increasing the predicted "bottom" stresses in hydrodynamic models, in reality the roughness would actually have the opposite effect on the sediment transport; that is, the roughness reduces bed shear stresses and thus suppresses sediment transport. While more research is required to develop robust predictive models of sediment transport in the presence of canopies, including how roughness modifies both the turbulent flow structure and bed shear stresses, as a starting point this study has demonstrated how reef roughness can result in a persistence of finer suspended sediments, lower SSCs and lower SSFs than would be predicted from using existing bare-bed sediment transport formulations.

## 6 Conclusions

The importance of sediment suspension and transport within coral reef ecosystems is well established; however, detailed measurements of sediment suspension and transport processes

in these environments have been historically very limited. Consequently, the physics employed to describe these processes is typically based upon principles developed for sandy beach environments that are extended to reefs with large roughness (canopies) without a firm theoretical basis. We show that such models are likely to inaccurately quantify (at even an order of magnitude level) both suspended sediment concentrations and sediment fluxes.

In this study, we conducted a detailed field experiment to investigate the turbulent flow structure, SSCs, rates of suspended sediment transport, and size distributions of suspended sediment in a coral reef environment under combined wave-current flow conditions. The key results of this study are as follows:

1. A clear logarithmic velocity layer developed above the reef canopy but did not extend into the canopy; instead the velocity profile was inflected and hence the flow was reduced in the roughness (canopy) region adjacent to the bed.
2. The shear stresses that arise from the large canopy drag forces imposed on the overlying flow do not represent the actual shear stress imparted on the underlying bed sediment. The actual shear stress is substantially smaller than that on a bare bed, as demonstrated by the fineness of the suspended fraction and low SSC concentrations, which could not have been predicted by traditional models.
3. Simple estimation of the wave and current shear stress above and within large roughness vastly improves the predictive capability of established formulae for the grain size and concentration of suspended sediment in reef systems. However, further research is required to improve predictions of the concentration profiles observed in this experiment (higher concentrations above the roughness than within it) and to develop robust sediment transport formulations that can be applied to coral reefs and other analogous ecosystem with large bottom roughness.

**Acknowledgements**

AWP is grateful for the support of a Robert and Maude Gledden Postgraduate Research Award and by The Gowrie Trust Fund (2013, 2014). This project was funded by the Western Australia Marine Science Institute (WAMSI) Dredging Science Node (Theme 2/3), an Australian Research Council Future Fellowship (FT110100201) and ARC Discovery Project grant (DP140102026) to RJL, as well as the U.S. Geological Survey's Coastal and Marine Geology Program. The authors thank Michael Cuttler, Sana Dandan, Jim Falter, Jeff Hansen, Malcolm McCulloch, Leonardo Ruiz Montoya, and Gundula Winter for their assistance during the experiment, and Johan Reyns for his assistance in the implementation of the advection-diffusion model. We thank Shawn Harrison at the USGS who conducted an internal review of this manuscript, as well as the two anonymous reviewers who provided constructive feedback that helped us to improve the manuscript. Data sets analyzed in this manuscript are available from http://doi.org/10.5281/zenodo.126670.

**References**


Ackerman, J. D., and A. Okubo (1993), Reduced mixing in a marine macrophyte canopy, *Functional Ecology*, *7*(3), 305-309, doi:10.2307/2390209.

Anthony, K. (2000), Enhanced particle-feeding capacity of corals on turbid reefs (Great Barrier Reef, Australia), *Coral Reefs*, *19*(1), 59-67.

Bagnold, R. (1966), An approach to the sediment transport problem from general physics, *US Geol. Surv. Prof. Pap.*, *422-I*, I1-I37.

Baptist, M. J. (2005), *Modelling floodplain biogeomorphology*, TU Delft, Delft University of Technology.

Bosman, J. J., E. T. J. M. van der Velden, and C. H. Hulsbergen (1987), Sediment concentration measurement by transverse suction, *Coast. Eng.*, *11*(4), 353-370, doi:10.1016/0378-3839(87)90033-0.

Bouma, T., L. van Duren, S. Temmerman, T. Claverie, A. Blanco-Garcia, T. Ysebaert, and P. Herman (2007), Spatial flow and sedimentation patterns within patches of epibenthic structures: Combining field, flume and modelling experiments, *Cont. Shelf. Res.*, *27*(8), 1020-1045.

Canny, J. (1986), A Computational Approach to Edge Detection, *Pattern Analysis and Machine Intelligence, IEEE Transactions on*, *PAMI-8*(6), 679-698, doi:10.1109/TPAMI.1986.4767851.

Chen, Z., A. Ortiz, L. Zong, and H. Nepf (2012), The wake structure behind a porous obstruction and its implications for deposition near a finite patch of emergent vegetation, *Water Resources Research*, *48*(9), doi:10.1029/2012WR012224.

Cuttler, M., R. Lowe, J. Hansen, J. Falter, and A. W. M. Pomeroy (2015), Grainsize, composition and beform patterns in a fringing reef system, *The Proceedings of Coastal Sediments*.

Finnigan, J. (2000), Turbulence in plant canopies, *Ann. Rev. Fluid. Mech.*, *32*(1), 519-571.

Francis, J. (1973), Experiments on the motion of solitary grains along the bed of a water-stream, *Proc.Roy.Soc.London, Series A*, *332*(1591), 443-471.

Francois, R., and G. Garrison (1982), Sound absorption based on ocean measurements. Part II: Boric acid contribution and equation for total absorption, *The Journal of the Acoustical Society of America*, *72*(6), 1879-1890, doi:10.1121/1.388673.

Gacia, E., T. C. Granata, and C. M. Duarte (1999), An approach to measurement of particle flux and sediment retention within seagrass (Posidonia oceanica) meadows, *Aquatic Botany*, *65*(1–4), 255-268, doi:10.1016/S0304-3770(99)00044-3

Ghisalberti, M. (2007), The impact of submerged canopies on open-channel hydrodynamics, *Proceedings of the 5th International Symposium on Environmental Hydraulics*.

Ghisalberti, M., and H. Nepf (2004), The limited growth of vegetated shear layers, *Water Resources Research*, *40*(7), W075021-W0750212.

Goring, D., and V. Nikora (2002), Despiking Acoustic Doppler Velocimeter Data, *J. Hydraul. Eng.*, *128*(1), 117-126, doi:10.1061/(ASCE)0733-9429(2002)128:1(117).

Grant, W. D., and O. S. Madsen (1979), Combined wave and current interaction with a rough bottom, *J. Geophys. Res. Oceans*, *84*(C4), 1797-1808.

Ha, H., J.-Y. Maa, K. Park, and Y. Kim (2011), Estimation of high-resolution sediment concentration profiles in bottom boundary layer using pulse-coherent acoustic doppler current profilers, *Mar. Geol.*, *279*(1-4), 199-209, doi:10.1016/j.margeo.2010.11.002

Hardy, T. A., and I. R. Young (1996), Field study of wave attenuation on an offshore coral reef, *J. Geophys. Res. Oceans*, *101*(C6), 14311-14326, doi:10.1029/96jc00202.

Hench, J. L., J. J. Leichter, and S. G. Monismith (2008), Episodic circulation and exchange in a wave-driven coral reef and lagoon system, *Limnol. Oceanogr*, *53*(6), 2681-2694.

Infantes, E., A. Orfila, G. Simarro, J. Terrados, M. Luhar, and H. Nepf (2012), Effect of a seagrass (Posidonia oceanica) meadow on wave propagation, *Marine Ecology Progress Series*, *456*, 63-72.

James, C., A. Jordanova, and C. Nicolson (2002), Flume experiments and modelling of flow-sediment-vegetation interactions, *International Association of Hydrological Sciences, Publication*(276), 3-9.

James, W. F., J. W. Barko, and M. G. Butler (2004), Shear stress and sediment resuspension in relation to submersed macrophyte biomass, *Hydrobiologia*, *515*(1-3), 181-191.

Jordanova, A., and C. James (2003), Experimental Study of Bed Load Transport through Emergent Vegetation, *J. Hydraul. Eng.*, *129*(6), 474-478, doi:10.1061/(ASCE)0733-9429(2003)129:6(474).

Kothyari, U. C., H. Hashimoto, and K. Hayashi (2009), Effect of tall vegetation on sediment transport by channel flows, *J. Hydraul. Res.*, *47*(6), 700-710.

Le Bouteiller, C., and J. Venditti (2015), Sediment transport and shear stress partitioning in a vegetated flow, *Water Resources Research*, *51*(4), 2901-2922.

Lee, G. h., W. B. Dade, C. T. Friedrichs, and C. E. Vincent (2004), Examination of reference concentration under waves and currents on the inner shelf, *J. Geophys. Res. Oceans*, *109*(C2).

Lowe, R. J., and J. L. Falter (2015), Oceanic Forcing of Coral Reefs, *Annu. Rev. Mar. Sci.*, *7*(18), 1-25, doi:10.1146/annurev-marine-010814-015834.

Lowe, R. J., J. L. Falter, M. D. Bandet, G. Pawlak, M. J. Atkinson, S. G. Monismith, and J. R. Koseff (2005a), Spectral wave dissipation over a barrier reef, *J. Geophys. Res. Oceans*, *110*(C04001), doi:10.1029/2004jc002711.

Lowe, R. J., J. L. Falter, S. G. Monismith, and M. J. Atkinson (2009a), A numerical study of circulation in a coastal reef-lagoon system, *J. Geophys. Res.*, *114*, C06022, doi:10.1029/2008jc005081.

Lowe, R. J., J. L. Falter, S. G. Monismith, and M. J. Atkinson (2009b), Wave-Driven Circulation of a Coastal Reef-Lagoon System, *J. Phys. Oceanogr.*, *39*, 873-893.

Lowe, R. J., J. Koseff, and S. G. Monismith (2005b), Oscillatory flow through submerged canopies: 1. Velocity structure, *J. Geophys. Res. Oceans*, *110*(C10016), 1-17, doi:10.1029/2004JC002788.

Lowe, R. J., U. Shavit, J. L. Falter, J. R. Koseff, and S. G. Monismith (2008), Modeling flow in coral communities with and without waves: A synthesis of porous media and canopy flow approaches, *Limnology and Oceanography*, *53*, 2668-2680, doi:10.4319/lo.2008.53.6.2668.

Luhar, M., S. Coutu, E. Infantes, S. Fox, and H. Nepf (2010), Wave-induced velocities inside a model seagrass bed, *J. Geophys. Res. Oceans*, *115*(C12).

Luhar, M., J. Rominger, and H. Nepf (2008), Interaction between flow, transport and vegetation spatial structure, *Environmental Fluid Mechanics*, *8*(5-6), 423-439, doi:10.1007/s10652-008-9080-9.

Neary, V. S., S. Constantinescu, S. Bennett, and P. Diplas (2011), Effects of vegetation on turbulence, sediment transport, and stream morphology, *J. Hydraul. Eng.*, *138*(9), 765-776.

Nepf, H. M. (2012), Flow and transport in regions with aquatic vegetation, *Ann. Rev. Fluid. Mech.*, *44*, 123-142.

Ogston, A. S., C. D. Storlazzi, M. E. Field, and M. K. Presto (2004), Sediment resuspension and transport patterns on a fringing reef flat, Molokai, Hawaii, *Coral Reefs*, doi:10.1007/s00338-004-0415-9.

Pomeroy, Andrew W. M. (2016), Tantabiddi Sediment Dynamics Experiment (Ninglaoo Reef): Hydrodynamic and suspended sediment data, *Zenodo*, Available from: http://doi.org/10.5281/zenodo.126670

Pomeroy, A. W. M., R. J. Lowe, G. Symonds, A. Van Dongeren, and C. Moore (2012), The dynamics of infragravity wave transformation over a fringing reef, *J. Geophys. Res. Oceans*, *117*(C11022), doi:10.1029/2012JC008310.

Presto, M. K., A. S. Ogston, C. D. Storlazzi, and M. E. Field (2006), Temporal and spatial variability in the flow and dispersal of suspended-sediment on a fringing reef flat, Molokai, Hawaii, *Estuarine, Coastal and Shelf Science*, *67*, 67-81, doi:10.1016/j.ecss.2005.10.015.

Prosser, I. P., W. E. Dietrich, and J. Stevenson (1995), Flow resistance and sediment transport by concentrated overland flow in a grassland valley, *Geomorphology*, *13*(1), 71-86.

Raupach, M. R., R. A. Antonia, and S. Rajagopalan (1991), Rough-Wall Turbulent Boundary Layers, *Applied Mechanics Reviews*, *44*(1), 1-25, doi:10.1115/1.3119492.

Richards, S., A. Heathershaw, and P. Thorne (1996), The effect of suspended particulate matter on sound attenuation in seawater, *The Journal of the Acoustical Society of America*, *100*(3), 1447-1450.

Rosman, J. H., and J. L. Hench (2011), A framework for understanding drag parameterizations for coral reefs, *J. Geophys. Res. Oceans*, *116*(C08025), doi:10.1029/2010jc006892.

Roth, M. S. (2014), The engine of the reef: photobiology of the coral–algal symbiosis, *Frontiers in microbiology*, *5*.

Shaw, W. J., and J. H. Trowbridge (2001), The direct estimation of near-bottom turbulent fluxes in the presence of energetic wave motions, *Journal of Atmospheric and Oceanic Technology*, *18*(9), 1540-1557.

Shields, A. (1936), Application of similarity principles and turbulence research to bed-load movement.

Smith, J. D., and S. McLean (1977), Boundary layer adjustments to bottom topography and suspended sediment, *Elsevier Oceanography Series*, *19*, 123-151.

Soulsby, R. (1997), *Dynamics of Marine Sands: A Manual for Practical Applications*, Thomas Telford, London.

Soulsby, R., and S. Clarke (2005), Bed shear-stresses under combined waves and currents on smooth and rough beds, *HR Wallingford, Report TR137*.

Storlazzi, C. D., M. E. Field, M. H. Bothner, M. K. Presto, and A. E. Draut (2009), Sedimentation processes in a coral reef embayment: Hanalei Bay, Kauai, *Mar. Geol.*, *264*, 140-151, doi:10.1016/j.margeo.2009.05.002.

Storlazzi, C. D., A. S. Ogston, M. H. Bothner, M. E. Field, and M. K. Presto (2004), Wave- and tidally-driven flow and sediment flux across a fringing coral reef: Southern Molokai, Hawaii, *Cont. Shelf. Res.*, *24*(12), 1397-1419, doi:10.1016/j.csr.2004.02.010.

Suhayda, J. N., and H. H. Roberts (1977), Wave action and sediment transport on fringing reefs, paper presented at 3rd International Coral Reef Symposium, Miami.

Symonds, G., K. P. Black, and I. R. Young (1995), Wave-driven flow over shallow reefs, *J. Geophys. Res.*, *100*, 2639-2648, doi:10.1029/94jc02736.

Van Dongeren, A., R. Lowe, A. Pomeroy, D. M. Trang, D. Roelvink, G. Symonds, and R. Ranasinghe (2013), Numerical modeling of low-frequency wave dynamics over a fringing coral reef, *Coast. Eng.*, *73*, 178-190, doi:10.1016/j.coastaleng.2012.11.004.

van Katwijk, M. M., A. R. Bos, D. C. R. Hermus, and W. Suykerbuyk (2010), Sediment modification by seagrass beds: Muddification and sandification induced by plant

cover and environmental conditions, *Estuarine, Coastal and Shelf Science*, *89*(2), 175-181, doi:10.1016/j.ecss.2010.06.008.

Van Rijn, L. C. (1984), Sediment transport, Part II: Suspended load transport, *J. Hydraul. Eng.*, *110*(11), 1613-1641.

Van Rijn, L. C. (1993), *Principles of sediment transport in rivers, estuaries and coastal seas*, Aqua publications Amsterdam, Amsterdam.

Van Rijn, L. C. (2007), Unified view of sediment transport by currents and waves. I: Initiation of motion, bed roughness, and bed-load transport, *J. Hydraul. Eng.*, *133*(6), 649-667.

Ward, L. G., W. M. Kemp, and W. R. Boynton (1984), The influence of waves and seagrass communities on suspended particulates in an estuarine embayment, *Mar. Geol.*, *59*(1), 85-103.

Weber, M., D. de Beer, C. Lott, L. Polerecky, K. Kohls, R. M. Abed, T. G. Ferdelman, and K. E. Fabricius (2012), Mechanisms of damage to corals exposed to sedimentation, *Proceedings of the National Academy of Sciences*, *109*(24), E1558-E1567.

Wiberg, P. L. (1995), A theoretical investigation of boundary layer flow and bottom shear stress for smooth, transitional, and rough flow under waves, *J. Geophys. Res. Oceans*, *100*(C11), 22667-22679.

Widdows, J., N. D. Pope, M. D. Brinsley, H. Asmus, and R. M. Asmus (2008), Effects of seagrass beds (Zostera noltii and Z. marina) on near-bed hydrodynamics and sediment resuspension, *Marine Ecology Progress Series*, *358*, 125.

Zeller, R. B., F. J. Zarama, J. S. Weitzman, and J. R. Koseff (2015), A simple and practical model for combined wave–current canopy flows, *Journal of Fluid Mechanics*, *767*, 842-880.

914 **Table 1:** Notation

| Symbol | Definition |
|---|---|
| $a$ | Frontal area per unit volume |
| $c$ | Concentration at elevation $z$ |
| $c_0$ | Reference concentration at elevation $z_{ref}$ above the bed |
| $d$ | Vertical height of momentum absorption above the bed |
| $g$ | Acceleration due to gravity |
| $h$ | Roughness height |
| $k_N$ | Non-dimensional Nikuradse roughness height |
| $s$ | Relative density of sediment in seawater |
| $\bar{u}$ | Mean velocity (current) |
| $\tilde{u}$,$\tilde{w}$ | Oscillatory velocity in maximal and upward directions |
| $u'$,$w'$ | Turbulent velocity maximal and upward directions |
| $u_* = \sqrt{\tau/\rho_w}$ | Shear velocity |
| $w_s$ | Particle fall velocity |
| $z$ | Elevation above the bed |
| $z_0$ | Bed hydraulic roughness length scale |
| $z_{0a}$ | Apparent bed roughness length scale due to wave-current interaction |
| A | Empirical coefficient |
| B | Empirical coefficient |
| $C_D$ | Drag coefficient |
| $C_f$ | Bottom friction coefficient |
| $D$ | Grain size of interest |
| $D_*$ | Dimensionless grain size |
| $D_{50}$ | Median grain size |
| $H$ | Wave height |
| $P$ | Rouse parameter |
| $T_p$ | Peak wave period |
| $z_{ref}$ | Height for reference concentration $c_0$ |
| $\alpha$ | Factor that accounts for the probability of sediment suspension |
| $\delta$ | Boundary layer thickness |
| $\varepsilon_s$ | Sediment mixing (diffusion) coefficient |
| $\theta$ | Grain size Shields parameter |
| $\kappa$ | Von Karman's constant ≈ 0.40 |
| $\nu$ | Kinematic viscosity of water |
| $\nu_t$ | (Turbulent) Eddy viscosity of water |
| $\rho_w$, $\rho_s$ | Density of sea water, density of sediment |
| $\tau$ | Horizontal shear stress |
| $\tau_{drag}$ | Shear stress due to bed roughness / features |
| $\tau_{grains}$ | Grain related shear stress |
| $\tau_{total}$ | Total resistance experienced by overlying flow |
| $\omega = 2\pi/T$ | (absolute) radian frequency of the waves |

**Subscripts**

| | |
|---|---|
| $bed$ | At the bed |
| $c$ | Current alone |
| $ig$ | Infragravity quantity (25s < T < 250s) |
| $m$ | Mean of the enhanced flow due to wave-current interaction |

| | |
|---|---|
| $max$ | Maximum of the oscillatory component of the enhanced flow due to wave-current interaction |
| $rms$ | Root-mean-squared quantity |
| $rough$ | At the top of the roughness layer (~ top of the canopy) |
| $sw$ | Sea-swell quantity (5s < T < 25s) |
| $w$ | Waves alone |
| $\infty$ | Free-stream velocity |

915

**Table 2.** Instrument site information and sampling configuration[#]

| Site and Depth | Instrument | Sampling Information |
|---|---|---|
| S1 (forereef ~10.5 m) | Nortek AWAC | 1 Hz with 2048 s burst every 3600 s; current profile every 5 min, 30 bins at 0.5 m; velocity sample height: 1.04 m |
| | RBRVirtuoso D | Continuous sampling at 1 Hz; pressure sample height: 0.2 m |
| S2 (reef flat ~1.5 m) | Nortek ADV | 8 Hz with 2048 s burst every 3600 s; velocity sample height: 0.23 m, 0.53 m and 0.85 m. |
| | Nortek ADP-HR | Continuous 1 Hz current profile, 31 cells at 25 mm, velocity sample height: 0.22 m; pressure sample height: 0.07 m |
| | Wetlabs FLNTU | 0.29 Hz with 462 samples every 3600 s; sample heights: 0.37, 0.64, 0.90 m |
| | Suction samples | Hourly during daylight; SSC sample heights: 0.22, 0.27, 0.34, 0.51, 0.76, 1.02 m. |

[#] Samples heights are relative to the seabed

**Table 3.** Calibration parameters used for the linear conversion of the ADP and OBS backscatter data ($B_k$) to suspended sediment concentrations (*SSC*). For the ADP, the nearest cell to the suction port was used in the calibration while the nearest port to the OBS sample cell was used for the OBS calibration.

| $z_{instrument}$ [#] [m] | $z_{port}$ [m] | Calibration Equation [mg $L^{-1}$] | $R^2$ | p | n |
|---|---|---|---|---|---|
| | | *ADP* | | | |
| 0.52 | 0.51 | $SSC = 0.052\ B_k - 2.68$ | 0.61 | <0.001 | 35 |
| 0.77 | 0.76 | $SSC = 0.062B_k - 3.25$ | 0.64 | <0.001 | 31 |
| 1.02 | 1.01 | $SSC = 0.067B_k - 3.53$ | 0.61 | <0.001 | 28 |
| | | *OBS* | | | |
| 0.37 | 0.34 | $SSC = -0.95B_k + 6.59$ | 0.76 | <0.001 | 10 |
| 0.64 | 0.76 | $SSC = -0.64B_k + 4.72$ | 0.73 | <0.001 | 11 |
| 0.90 | 1.02 | $SSC = -2.73B_k + 9.52$ | 0.51 | 0.109 | 5 |

[#]cell height corrected for difference in bathymetry between suction sample ports and ADP which is estimated to be ~0.20 m.

**Figure 1.** Conceptual model of the boundary layer flow structure for (top) bare beds and (bottom) beds with large roughness under (left) unidirectional (current) and (right) wave-dominated (oscillatory) flow conditions.

**Figure 2.** (a) The location of Tantabiddi within Ningaloo Reef in northern Western Australia. (b) An aerial view of the site in site (origin: 21.89248°S, 113.96203°E) with the location of the instruments relevant to this study and key contours indicated. (c) Interpolated sonar bathymetry around the high-resolution sampling site on the reef flat relative to the mean water level, with the mean flow direction indicated. The dashed line indicates the cross-reef direction. (d) Bathymetry transects measured perpendicular to the sawhorse frame from south to north and relative to the location of the vertical ADV array (blue dots). The vertical line indicates the vertical range of the ADP profiler within the vertical scale of the figure. The arrow denotes the mean flow direction during the experiment. (e) Schematic illustration of the sawhorse frame deployed in the experiment and (f) an underwater image of the site with the deployed instrumentation.

**Figure 3.** A logarithmic fit of Eq. (2) (red) to the mean of the individual 15-min time-averaged velocity profiles measured during the experiment. The velocity measurements are normalized by the velocity measurement closest to the bed. The red dots denote the points used in the fit and the horizontal dashed line indicates 0.4 m above the bed, the approximate height of the roughness observed at the site.

**Figure 4.** The forereef S1 (a) water depth and (b) swell root-mean-squared (RMS) wave height $H_{rms,sw}$ and peak wave period $T_p$, along with the intensive sampling reef flat S2 site (c) water depth, (d) sea-swell ($H_{rms,sw}$, red) and infragravity ($H_{rms,ig}$, blue) RMS wave height, the (e) free-stream velocity defined as the depth-averaged velocity above the identified logarithmic region and (f) the relative importance of the free-stream mean flow versus the

RMS wave-induced flow. The dashed horizontal line indicates the threshold above which the conditions are current-dominated.

**Figure 5.** (a) The shear velocity $(u_{*m,rough})$ estimated from the middle ADV Reynolds stress (red) compared with the $u_{*m,rough}$ estimated from the ADP time-averaged velocity profiles with Eq. (1) (black). (b) $u_{*m,rough}$ as a function of the free-stream velocity $(\bar{u}_\infty)$. The colorbar denotes values of the roughness length scale $(z_{0a})$ (d) The roughness length scale $(z_{0a})$ as a function of the current-wave ratio $(\bar{u}_\infty/\tilde{u}_{rms})$. Note that all values in (b) and (c) are based on estimates from the ADP data.

**Figure 6.** Mean current $(\bar{u})$ profiles for (a) current- and (b) wave-dominated conditions along with RMS velocity $(\tilde{u}_{rms})$ profiles for (c) current- and (d) wave-dominated conditions. For all profiles, the ADP measurements are shown in red and the ADV measurements are shown in black with the horizontal error bars denoting ±1 standard deviation. The mean current profiles have been normalized by the free-stream current $(\bar{u}_\infty)$ and the RMS velocity profiles have been normalized by $\tilde{u}_{rms}$ above the roughness.

**Figure 7.** (a) The mean shear velocity at the bed $(u_{*m,bed})$ compared to the mean shear velocity at the top of the roughness $(u_{*m,rough})$. (b) The maximum shear velocity at the bed $(u_{*max,bed})$ compared to the maximum shear velocity at the top of the roughness $(u_{*max,rough})$. (c) $u_{*m,bed}$ compared to $u_{*max,bed}$.

**Figure 8.** Grain size distribution from (a) suction samples obtained at the port closest to the bed ($z$ = 0.23 m) and (b) determined from a bed surface sample obtained on the reef flat at S2. The histogram in (a) represents the distribution from a sample obtained at 15:00 on 2 August 2013 (local time). The vertical lines indicate the equivalent sediment diameter that could be suspended by the mean $(u_{*m,bed})$ (solid blue) and maximum $(u_{*max,bed})$ (dashed blue)

wave-induced bed shear velocities, and the mean shear velocity $(u_{*m,rough})$ (solid red) at the top of the roughness (canopy) layer. Note that the equivalent grain size that could be maintained in suspension by the maximum wave-induced shear velocity $(u_{*max,rough})$ at the top of the roughness layer is ~830 μm and is not indicated on the figure. The maximum (grey) and mean (black) shear velocity at the top of the roughness layer (c) and within the roughness layer (d) are shown for the entire experiment. The horizontal dashed line indicates the shear velocity required to suspend the median bed grain size, while the solid black line indicates the shear velocity required to suspended the median grain size observed in the suction samples.

**Figure 9.** Suspended sediment concentration (SSC) time series measured at (a) $z$ = 0.82 m, (b) $z$ = 0.52 m and (c) $z$ = 0.29 m above the bed. The black dots indicate the SSC estimated from the calibrated ADP, blue dots the OBS backscatter and the red dots indicate the directly measured SSC from the suction samples. The mean SSC profile measured by the calibrated ADP (black line) and directly from the suction samples (red dots) for the forereef conditions: (d) low waves and rising tide (note: no suction samples were obtained for this condition), (e) low waves and falling tide, (f) high waves and rising tide and (g) high waves and falling tide. The vertical dotted lines and error bars indicate one standard deviation in the measured data. The horizontal dotted line indicates the approximate height of the roughness.

**Figure 10.** Depth-integrated suspended sediment concentration (SSC) within the roughness $(z = 0.2 - 0.4\text{m})$ determined from the ADP backscatter compared to the mean bed shear velocity (blue) and maximum bed shear velocity (red).

**Figure 11.** (a) Sediment mixing (diffusion) profile $(\varepsilon_s)$ used in the advection-diffusion model. (b) Suspended sediment concentration (SSC) profiles from the advection-diffusion model with the concentration $(c)$ normalized by the upstream boundary concentration $(c_{x=0})$.

994 (black) no roughness layer in the model and (red) with a roughness layer in the model. The
995 horizontal dotted line denotes the approximate height of the roughness in the model.

996 **Figure 12.** (a)-(d) Suspended sediment flux (SSF) on the reef flat compared with the SSF
997 estimated using a power-law profile with the reference concentration ($C_o$) formulation of *Lee*
998 *et al.* [2004], $D_{50}$ = 70 μm or 240 μm and (top) $u_{*max,rough}$ and (middle) $u_{*max,bed}$. The solid
999 black line indicates 1:1 agreement. (e) Estimated SSF (red) and measured SSF (black) for the
1000 duration of the experiment.

**Figure 1.**

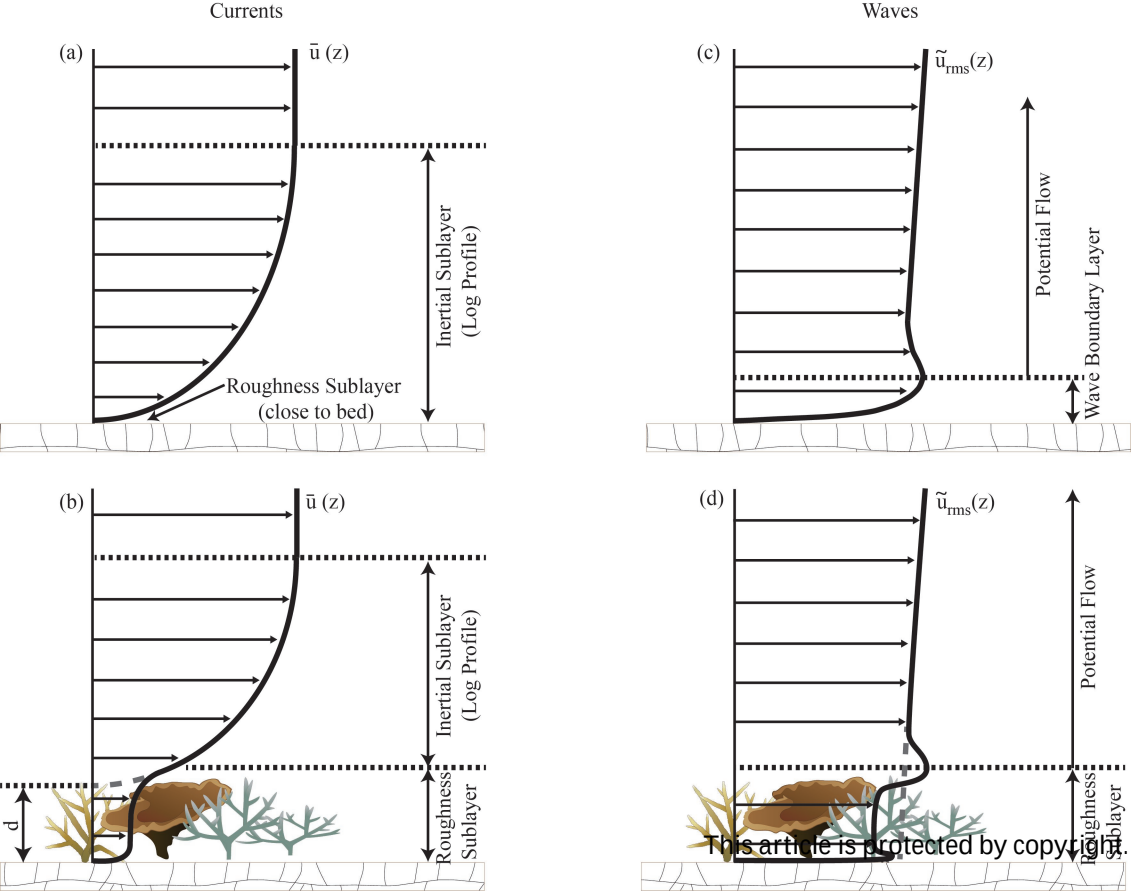

**Figure 2.**

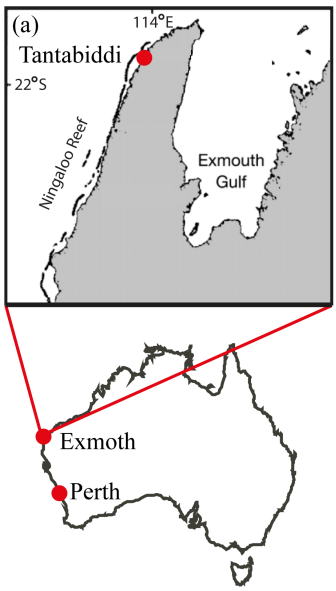


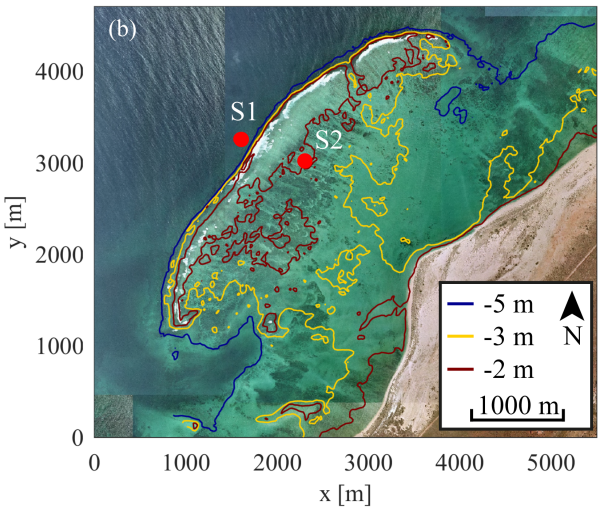


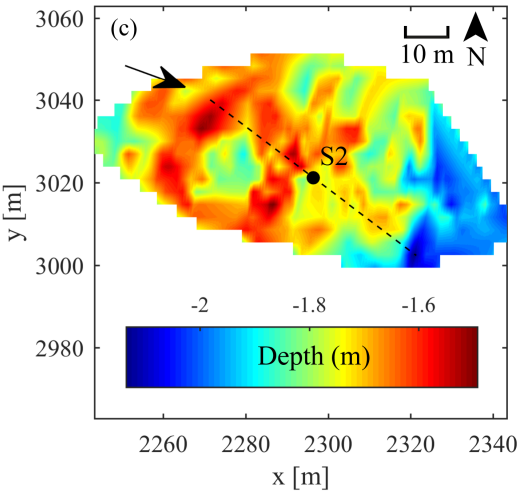


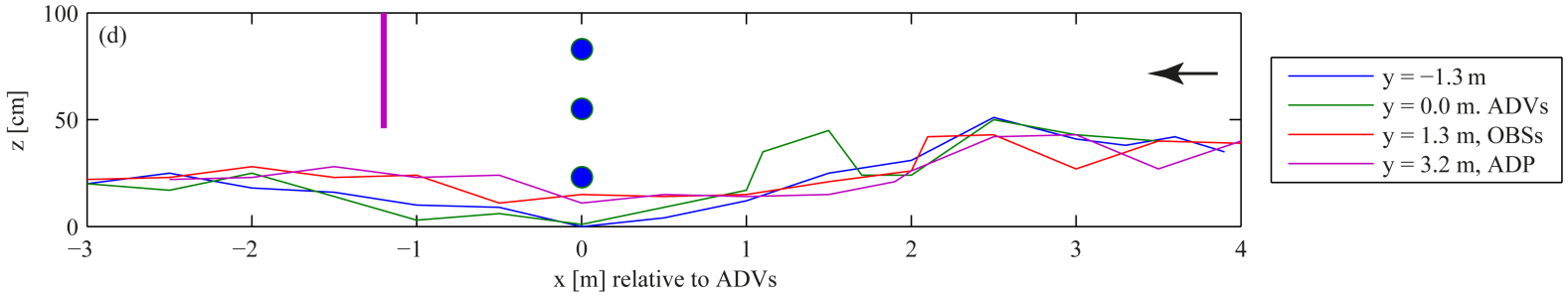


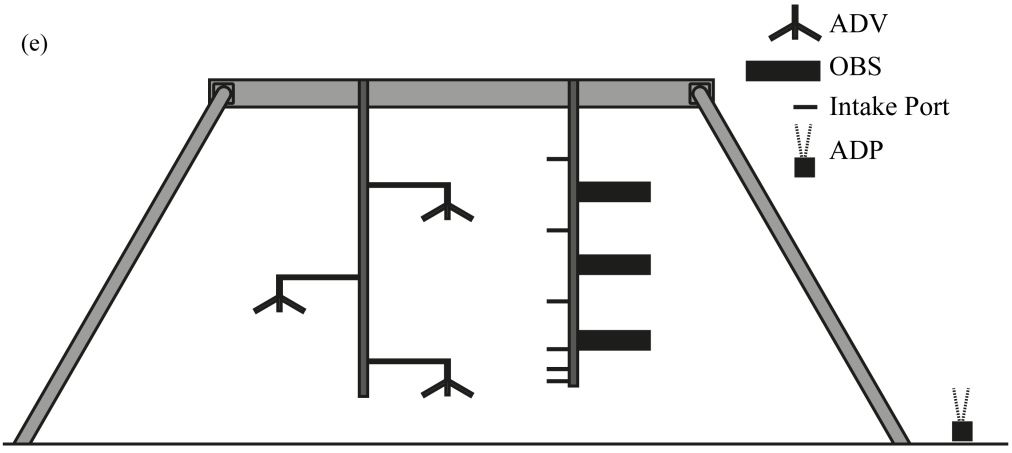


**Figure 3.**

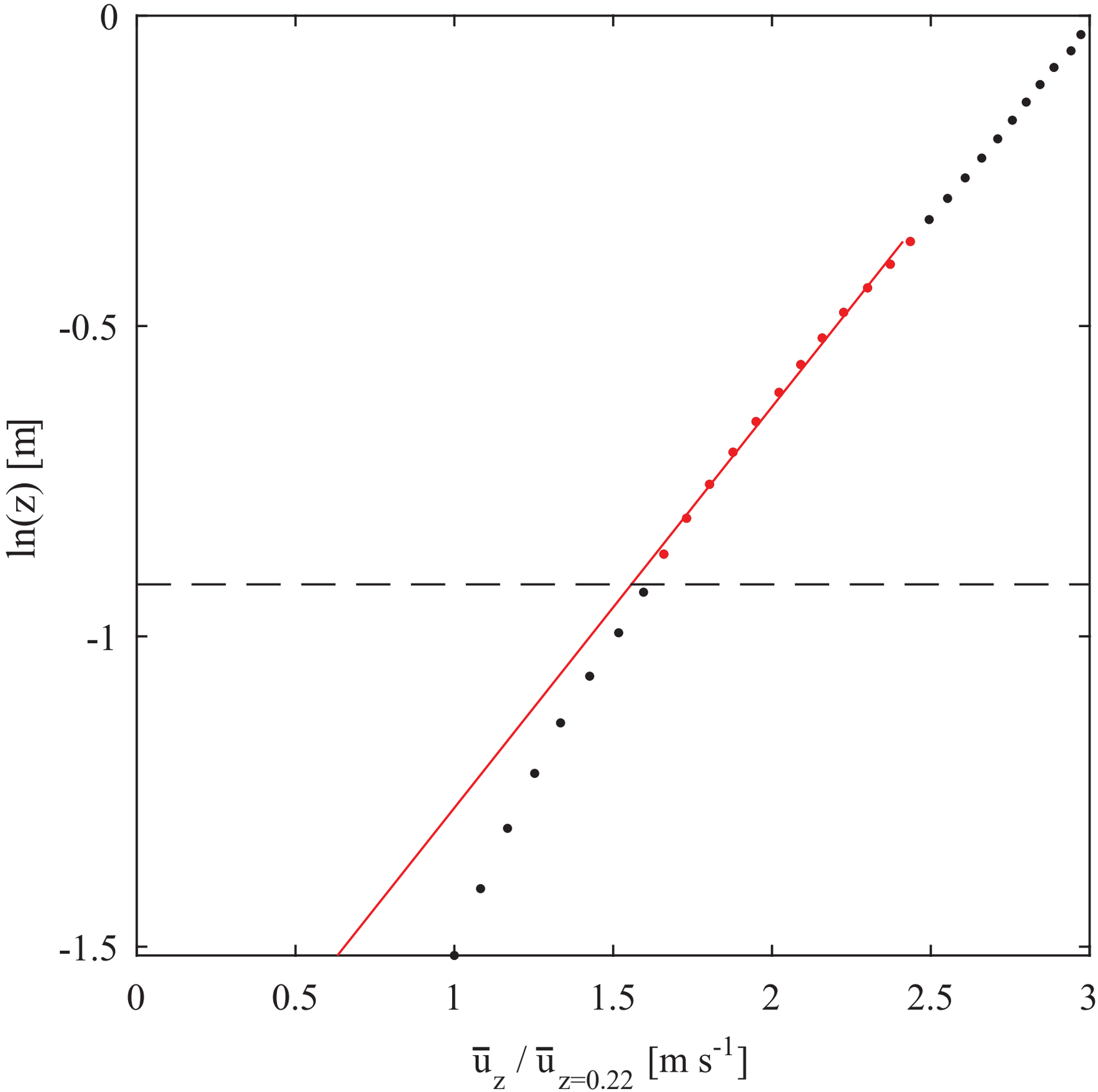
0
-0.5
-1
-1.5
ln(z) [m]
0
0.5
1
1.5
2
2.5
3
$\bar{u}_z / \bar{u}_{z=0.22}$ [m s$^{-1}$]

**Figure 4.**

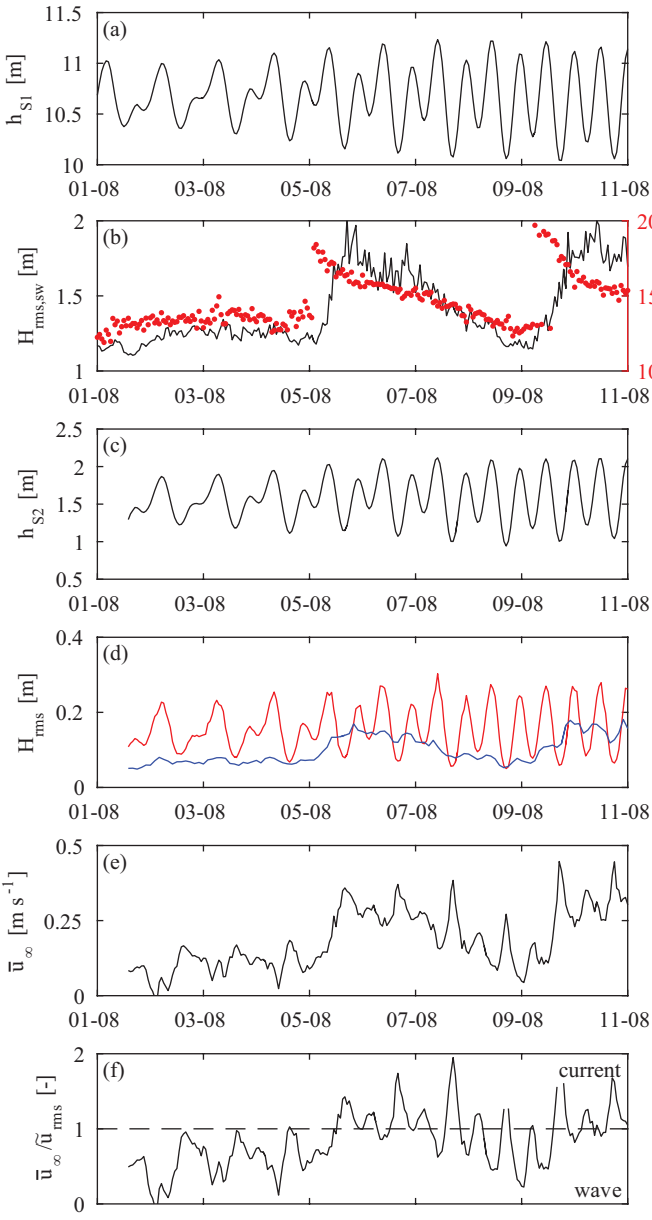

**Figure 5.**

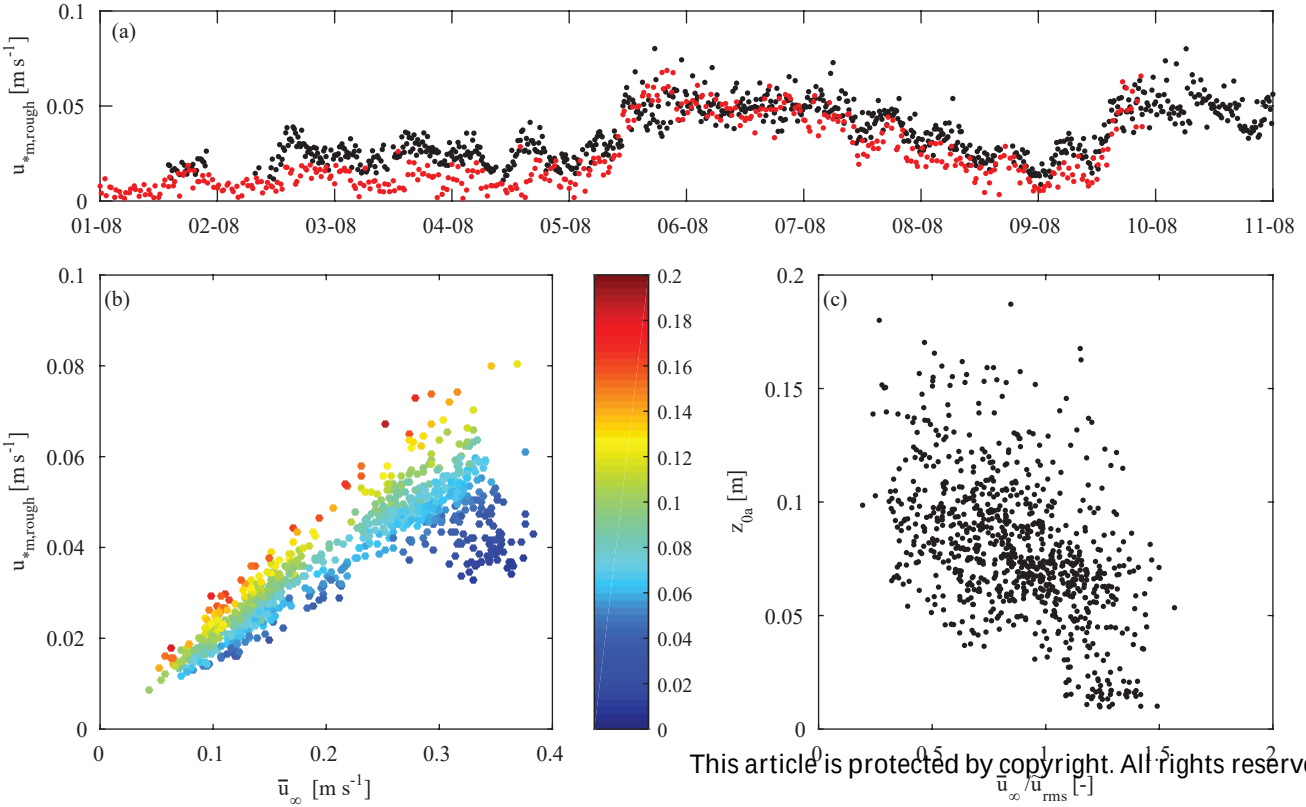

**Figure 6.**

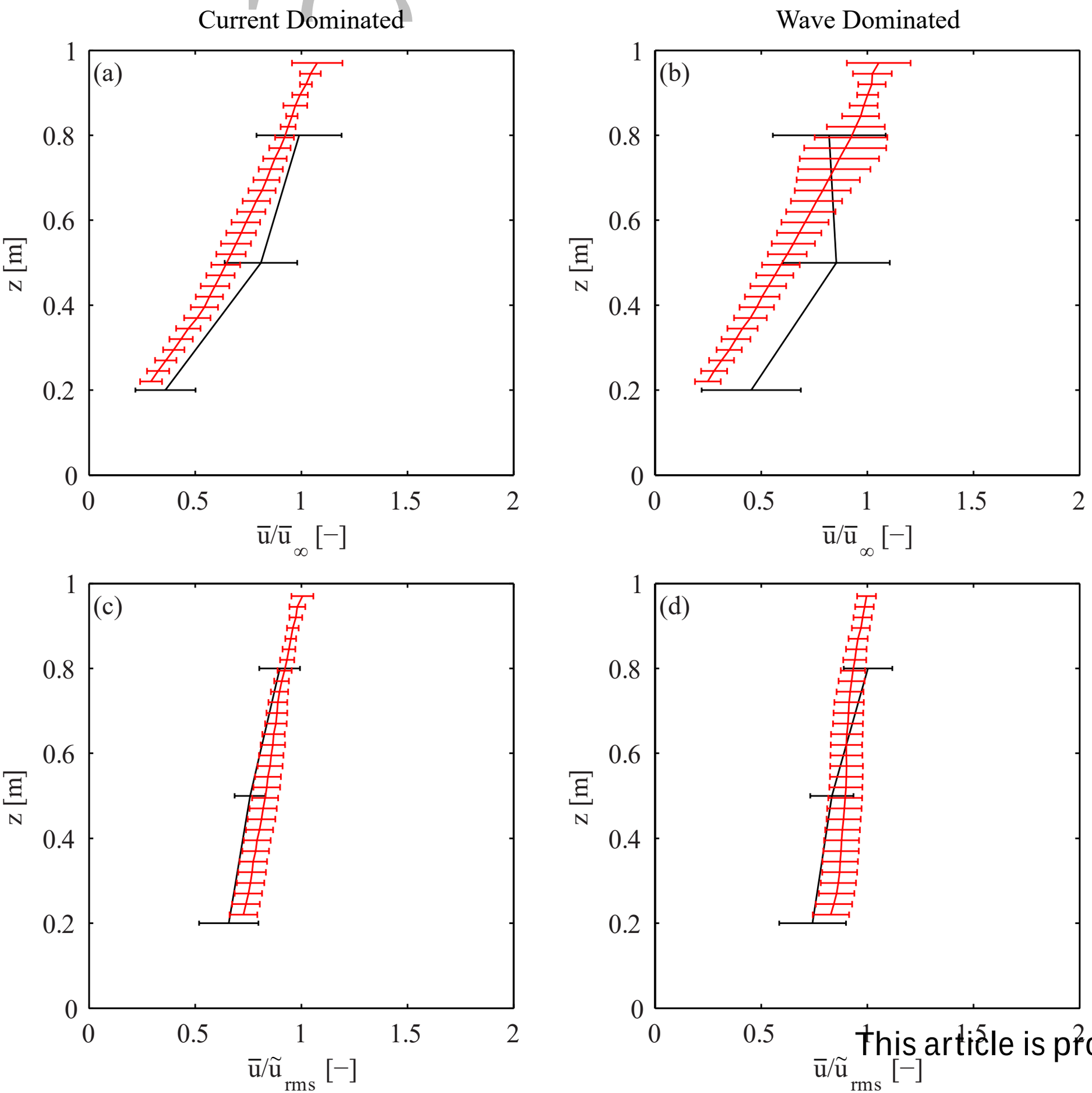

**Figure 7.**

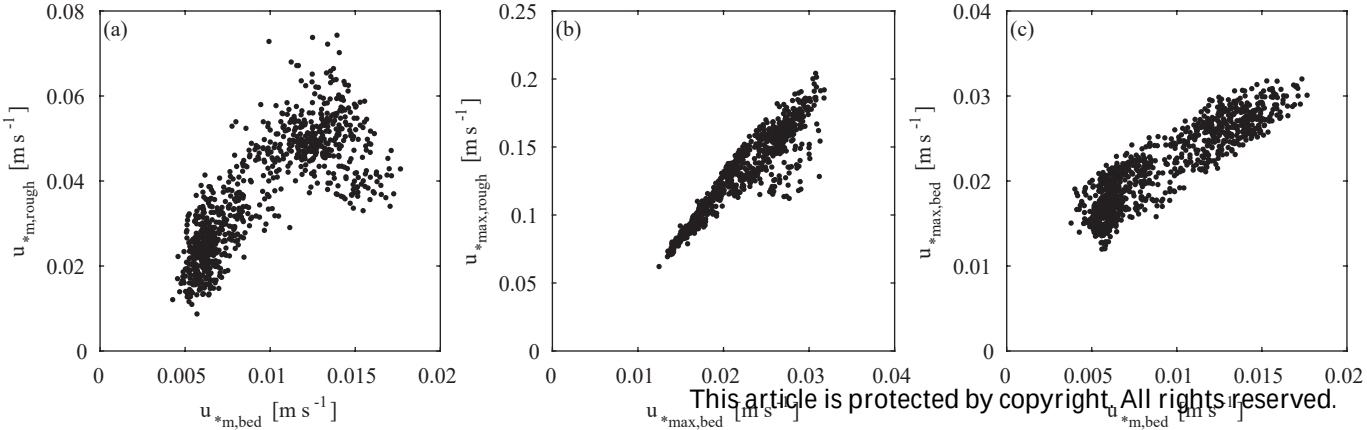

**Figure 8.**

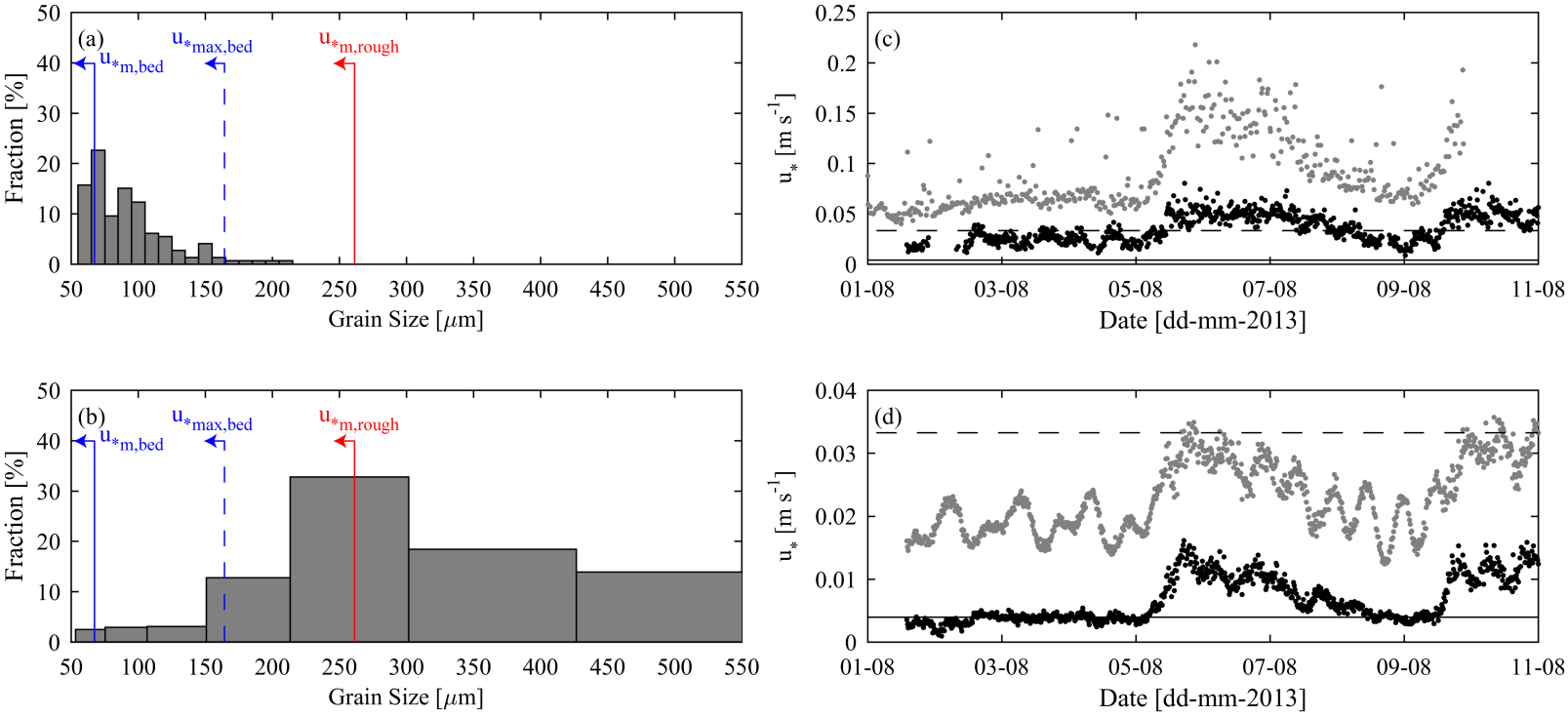

**Figure 9.**

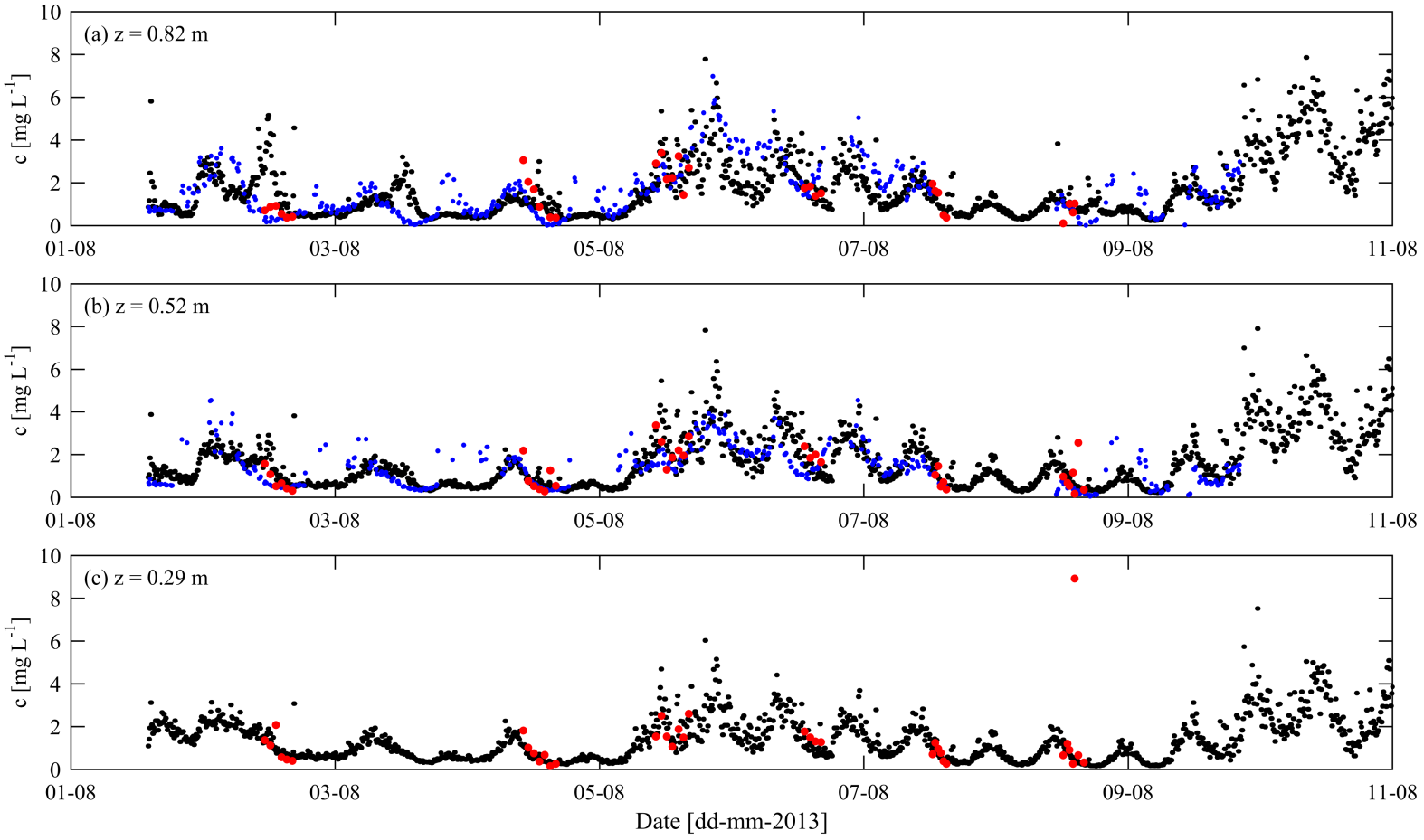


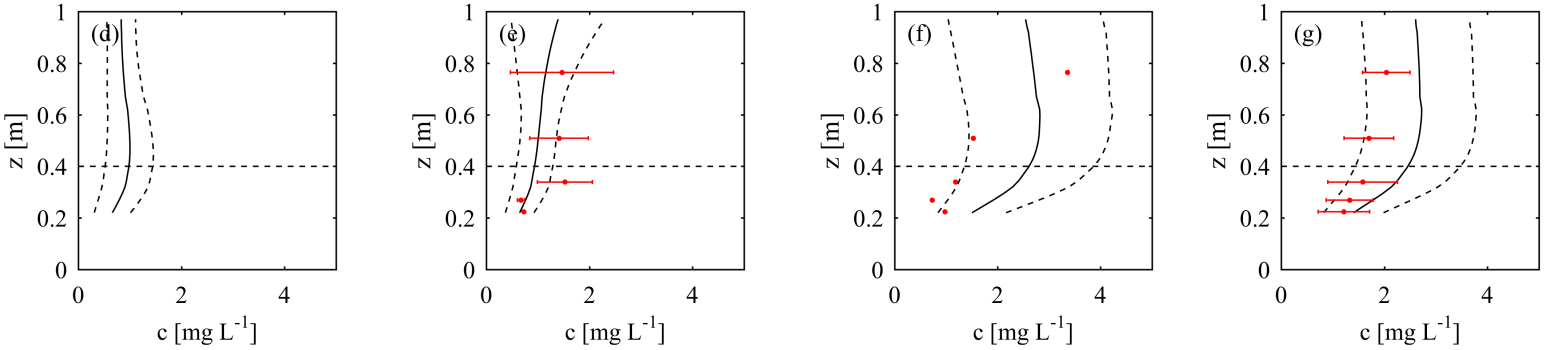

**Figure 10.**

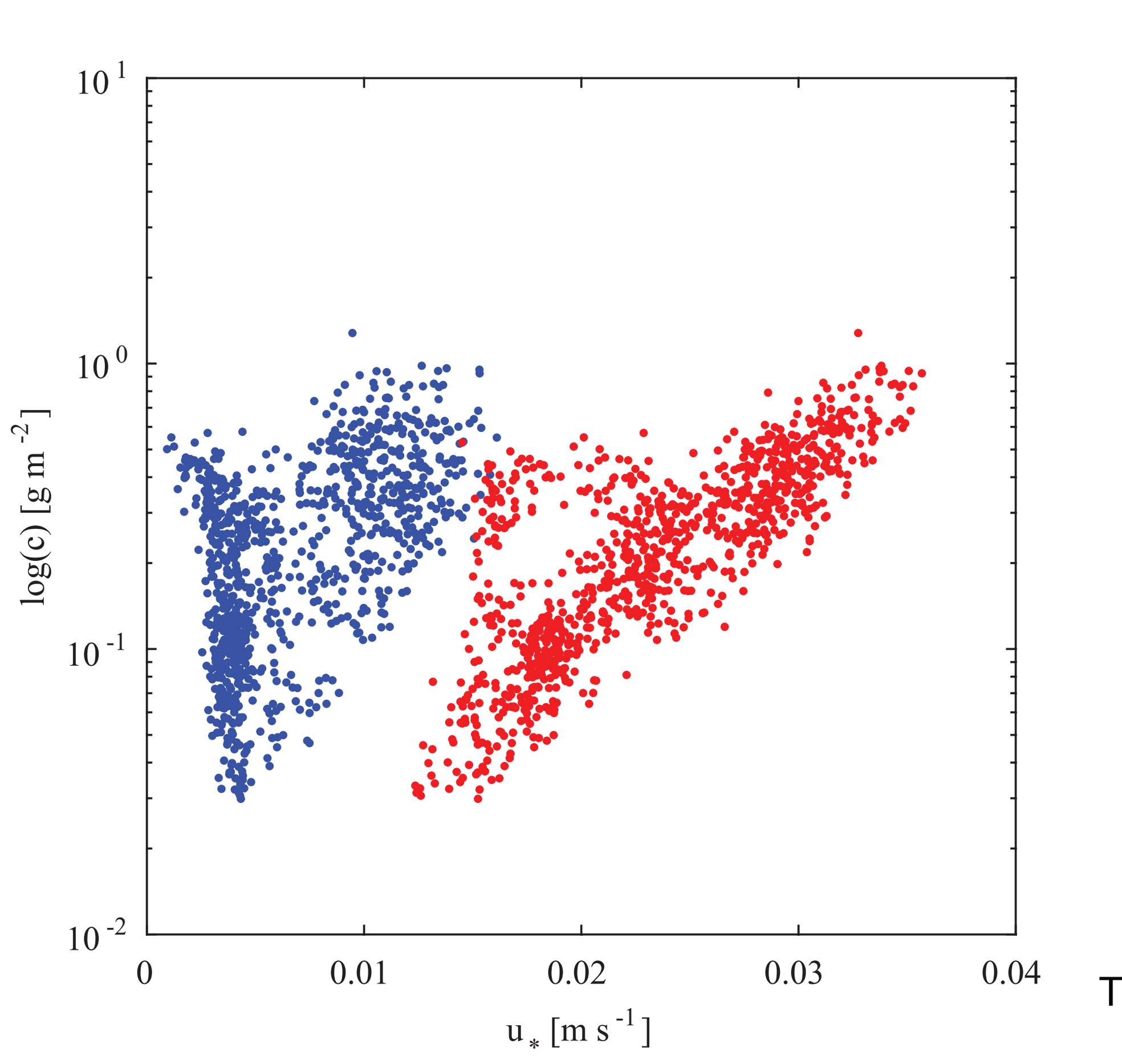
10 1
10 0
10 -1
10 -2
log(c) [g m -2]
0
0.01
0.02
0.03
0.04
u * [m s -1]

**Figure 11.**

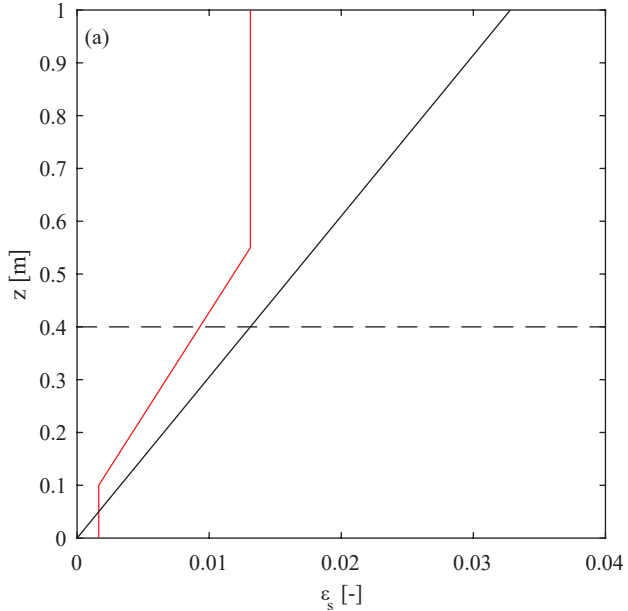


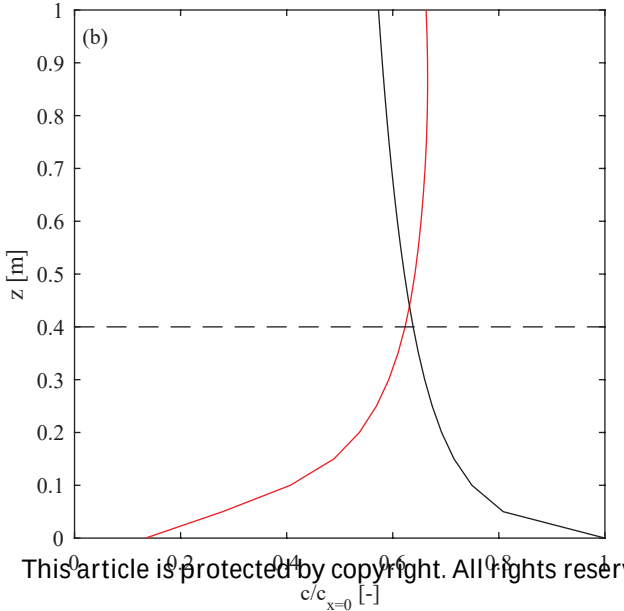

**Figure 12.**